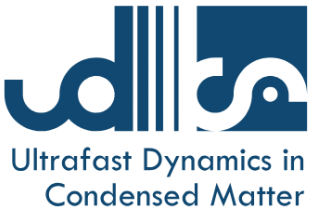

Investigation of surface plasmon polaritons on gold nanotriangles

Gregor E. Stockmann

Universitätsmasterarbeit
zur Erlangung des akademischen Grades

Master of Science
(M.Sc.)

im Studiengang
Physik

eingereicht am 20. Januar 2025
in der Arbeitsgruppe Ultraschnelle Dynamik
in kondensierter Materie
am Institut für Physik und Astronomie
der Universität Potsdam

Betreuer

Dr. Felix Stete
University of Potsdam

Gutachter

Prof. Dr. Matias Bargheer
University of Potsdam

Prof. Dr. Svetlana Santer
University of Potsdam

Abstract

Ever since the discovery of surface plasmon polaritons (SPPs), it has been a goal to employ their various forms of energy transport for catalytic purposes regarding chemical reactions. Fundamental research to uncover all relevant mechanisms is still in progress. However, because SPPS are photoexcited, it can be difficult to distinguish their influence on a chemical reaction from direct laser excitation. To quantify only the contribution of SPPs to a chemical reaction, spatial separation of excitation- and reaction site is elementary. One way to achieve spatial separation is to use certain forms of metallic structures on the micrometre scale, such as gold triangles. Within this master thesis, an experimental setup to excite and investigate surface plasmon polaritons on gold triangles is developed and implemented.
The base side of the triangle is illuminated with laser light in order to excite surface plasmons. These, in turn, propagate along the air/gold interface and are focused at the tip due to the tapered shape of the triangle. At the tip, the plasmons can decouple again in the form of light. Confirmation of plasmonic excitation is achieved by the thorough analysis of the decoupled light.

The experimental setup is based on an optical microscope that is adapted and extended during the study. Notable improvements included the capability to excite the sample with a broadband white light laser under grazing incidence, the option to choose between a visible- and infrared-optimised beam path, and the integration of a mechanism to physically select the examination area. This setup enables the analysis of a region of interest both in an intensity-dependent and spectrally resolved manner. The optimised setup described above substantially facilitates the verification of the plasmonic origin of the emitted light at the tip. As part of the research, the intensity of light emission was investigated as a function of polarisation and excitation wavelength. Results for the former measurements follow known theoretical concepts. For the latter measurements, corrections regarding setup influences, such as the excitation spectrum and the losses caused by the experimental setup, are necessary to find an agreement with the literature.

Zusammenfassung

In der vorliegenden Arbeit wird das Propagationsverhalten von Oberflächen-Plasmonen-Polaritonen an Golddreiecken auf der Mikrometer-Skala untersucht. Das Ziel ist die Entwicklung eines Aufbaus zur störungsfreien Untersuchung von plasmonische getriebenen chemischen Reaktionen. Zu diesem Zweck wird die räumliche Trennung des Anregungsorts vom Reaktionsort durch den Einsatz propagierender Oberflächenplasmonen angestrebt. Zur Umsetzung wird die Basisseite des Dreiecks mit Laserlicht angeregt. An der Kante regt das einfallende Licht Oberflächenplasmonen an, welche wiederum entlang der Luft/Gold-Grenzfläche propagieren und durch die zulaufende Form des Dreiecks an der Spitze fokussiert werden. Im Anschluss können die Plasmonen an der Spitze wieder in Form von Licht auskoppeln. Im Rahmen dieser Arbeit wurde ein experimenteller Aufbau konzipiert und realisiert, um einerseits propagierende Oberflächenplasmonen an der Basiskante eines Golddreiecks zu stimulieren und andererseits die plasmonenbasierte Lichtemission an der Spitze zu analysieren.

Die Grundlage des Aufbaus bildet ein optisches Mikroskop, das im Rahmen der Arbeit angepasst und erweitert wurde. Besonders hervorzuheben sind die folgenden Erweiterungen: Die Möglichkeit der Anregung mit einem breitbandigen Weißlichtlaser unter flachem Einfallswinkel (Grazing Incidence), die Wahl zwischen einem sichtbaren- und infrarot-optimiertem Strahlengang und die Integration eines Aufbaus zur physischen Selektion eines Untersuchungsbereichs. Abschließend besteht die Möglichkeit, den Interessensbereich sowohl intensitätsabhängig als auch spektral aufgelöst zu analysieren. Der zuvor beschriebene Aufbau ermöglichte die Durchführung einer Vielzahl von Untersuchungen, die darauf abzielten, die Hypothese zu verifizieren, ob die Lichtemission an der Spitze plasmonischen Ursprungs ist. Im Rahmen der Analyse wurden die Intensität der Lichtemission in Abhängigkeit von der Polarisation sowie der Wellenlänge des Anregungslichts untersucht. Darüber hinaus erlaubt diese Konfiguration eine spektrale Analyse unter Berücksichtigung des Anregungsspektrums und der Verluste, die durch den experimentellen Aufbau entstehen.

Contents

Abbreviations

fig.	figure
sec.	section
ch.	chapter
SPP	surface plasmon polariton
SPPs	surface plasmon polaritons
pSPPs	propagating surface plasmon polaritons
CE	coupling efficiency
DE	decoupling efficiency
VIS	visible
IR	infrared
NIR	near-infrared
UV	ultraviolet
AFM	atomic force microscope
ROI	region of interest
AOI	angle of incidence
WL	white light
GI	grazing incidence
CRC	Collaborative Research Center
S/N	signal-to-noise ratio
NP	nanoparticle
LS	laser spectrum
LSS	laser-system-spectrum

Formula symbols

ϵ_0	vacuum permittivity
ϵ	relative permittivity
ϵ_d	permittivity of the dielectric
ϵ_{metal}	permittivity of the metal
n	refraction index
κ	extinction coefficient
α	polarisability
E	electric field
P	polarisation
p	dipole moment
χ	susceptibility
n_V	unit volume
λ	wavelength
ω	frequency
ω_{SPP}	surface plasma frequency
ω_P	plasma frequency
k_{SPP}	SPP momentum vector
λ_{SPP}	SPP wavelength
δ_{i}	penetration depth
L	propagation length

1 Introduction

A surface plasmon polariton (SPP) can be defined as an electromagnetic excitation that propagates like a wave along a metal-dielectric interface. It is characterised by an evanescent nature perpendicular to the interface, meaning that the amplitude decays exponentially with increasing penetration depth into each material. Under the right circumstances, SPPs can travel several hundreds of micrometers along the interface at almost the speed of light [1] [2] [3] [4]. The exceptional properties of SPPs offer a wide range of applications in research, science, and technology. In recent years, SPPs have become very important in several areas. SPPs are used in biotechnology as bio-sensors [5] and in medicine. In the field of spectroscopy, for example, they are utilised to amplify Raman scattering [6] and enhance molecular fluorescence spectroscopy [7]. A significant research area involves the application of SPPs with nanoscale devices, particularly in thin metal films and nanostructures. This offers numerous possibilities in optoelectronics and nanotechnology, as evidenced by the development of surface plasmon-based nano-circuits [8] and optical waveguides operating on sub-wavelength scales [9] [10] [11]. The recent funding of the Collaborative Research Center 1636 (CRC1636), which is dedicated to elementary processes of light-driven reactions at nanoscale metals, demonstrates the increased level of interest in this field in recent years [12].

The project A06 of the CRC investigates the potential of propagating SPPs (pSPPs) to drive and influence chemical reactions. The key idea is the separation of excitation and reaction sites by using pSPPs to transport energy along metallic nanostructures such as thin films [13] or nanowires [14]. The chemical reaction is driven exclusively by plasmons, enabling its undisturbed observation without the influence of scattered light or laser-deposited heat from an excitation laser at the reaction site.

The objective of this study is to construct an experimental setup for the excitation and observation of pSPPs on gold micro-triangles. The proposed approach involves the SPP excitation at the gold triangle's base side with a tunable VIS-IR laser. The SPPs subsequently propagate along the air/gold interface and are focused by the triangular shape at the tip. At the tip, the SPPs scatter and couple out of the triangle in the form of light. With the help of the system I have built, the emitted light can be observed and investigated. In the further framework, fundamental properties of the excited SPPs, such as polarisation, wavelength dependence, and propagation behaviour, are analysed and discussed.

Outline

This master thesis is structured as follows:
The second chapter provides a comprehensive overview of the theoretical fundamentals of propagating surface plasmon polaritons, with particular attention to the properties of SPPs, including their propagation length and penetration depth. The final sections of this chapter cover the SPP excitation and coupling. Initially, the theoretical underpinnings of the excitation methods are delineated. Subsequently, the efficiencies of the light-SPP interaction at the base and tip of the sample are evaluated.
Chapter 3 is concerned with the description of the methods and experimental approaches that were developed and tested. It commences with a brief description of the gold triangle sample. Subsequently, the various expansions and modifications to the experimental setup are elucidated. The progression involves a transition from a rudimentary microscope configuration to a highly sensitive microscope equipped with a grazing incidence white light excitation.
Chapter 4 discusses the experimental results, focusing on the plasmon-based light emission at the triangle tip. Initially, polarisation- and wavelength-dependent measurements of the light were conducted to confirm the basic properties of SPPs, as established in analogous experiments. The subsequent spectral measurements of the light emission aim to obtain detailed information on the SSP distribution that reaches the tip. It is imperative to select the appropriate correction function. The chapter concludes with a concise overview of further improvement possibilities to these measurements.
The final chapter of the work offers a comprehensive conclusion, providing a synopsis of forthcoming approaches and investigations.

2 Theory of surface plasmon polaritons

As mentioned in the introduction, the fundamental concept is the energy transport along a gold nano-triangle via pSPPs to separate the excitation and reaction sites. Therefore, the first part of this chapter will describe the nature of plasmons, with particular emphasis on pSPPs.
The subsequent section discusses the origin of the SPP properties. The later investigated properties, such as penetration depth and propagation length, are based on the dielectric functions of the triangle material and the environment and the SPP dispersion relation along the interface.
The final part of this section will explain the different methods used to excite pSPPs, with particular reference to the method used to excite the pSPPs on a sharp-edged structure, such as the back of the triangles.

2.1 Surface plasmon polaritons

A plasmon is defined as a fundamental solid-state excitation in metals and describes the collective and resonant oscillation of free electrons. There are three major types of plasmons: Firstly, **Bulk plasmons**, which describe the collective oscillation of the free electron cloud in a homogeneous bulk metal [15]. Secondly, **localised plasmons**, which are the localised in small metal nanoparticles [15].

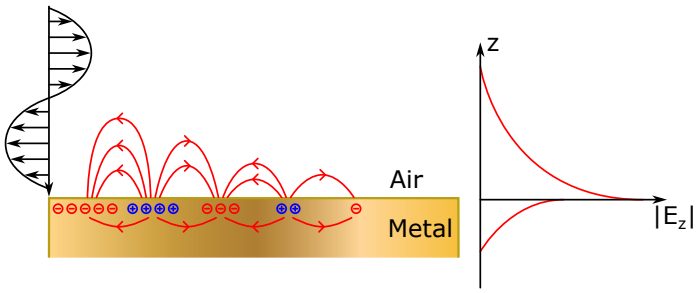

Figure 2.1: Left: Surface plasmon polariton (SPP) at an air-metal interface excited by a laser focused on the metal edge. Surface near charges are displaced antiparallel to the electric field vector. Due to coulomb forces, the displacement of charges propagates along the interface. **Right:** Penetration depth of the SPP electric field into the dielectric (air) and metal (gold)

The third and for this work relevant group are **surface plasmon polaritons** (SPPs). SPPs are collective oscillations of charge densities parallel to the dielectric/metal interface. Figure 2.1 displays a schematic representation of an SPP after the excitation by an external electromagnetic field. At the excitation side, an incident electric field displaces the free surface-near electrons in the metal in respect to the heavy ions. This leads to the collective oscillation of the electrons in resonance to the electric field. The movement of the electrons creates areas of different charge carrier concentrations. Consequently, electric fields are formed between these areas at both sides of the interface, in the dielectric and the metal. The propagation behaviour of the SPP is caused by the Coulomb interaction with neighboring charge carriers situated close to the excitation side. These also begin to oscillate and, in turn, interact with surrounding electrons. This creates a surface-near electromagnetic wave, which propagates with a periodically changing electric field along the surface. With increasing propagation distance along the interface, the intensity of the SPP decays due to loss processes in the metal. The decay follows the exponential decay of the Beer–Lambert law. The distance, where the intensity decayed by the factor of 1/e, is called the propagation length and is one of the key properties of this work. This will be further discussed in section 2.2.3.
As discussed earlier, the movement of the electrons leads to the formation of periodically changing electric fields at the interface. These fields decay evanescently perpendicular to the interface. and is called the penetration depth of a surface plasmon [1] [2] [3].

2.2 Properties of SPPs

In the previous section, it was outlined that an external electromagnetic (EM) wave displaces the electrons in the metal. This displacement builds up an electric dipole with an induced dipole moment

$$p = \epsilon_0 \alpha(\omega) E \tag{2.1}$$

where ϵ_0 is the vacuum permittivity and $\alpha(\omega)$ the frequency-dependent polarisability. The sum over all dipole moments per unit volume n_V leads to the polarisation $\mathbf{P}$

$$\mathbf{P} = \epsilon_0 n_V \alpha(\omega) E \tag{2.2}$$

The relation between the polarisation and the electric field $P = \epsilon_0 \chi E$ gives

$$\chi(\omega) = n_V \alpha(\omega) = \epsilon(\omega) - 1 \tag{2.3}$$

The permittivity $\epsilon(\omega)$, otherwise known as the dielectric function, is expressed as a complex function, $\epsilon(\omega) = \epsilon_1(\omega) + i\epsilon_2(\omega)$, with a real and an imaginary part. The real part ϵ_1 describes the material response to an electromagnetic field. From a larger $\epsilon_1(\omega)$ follows a larger polarisation and so an easier displacement of the charge carriers.
The imaginary part ϵ_2 describes the absorption of the material. In comparison to the real part, the imaginary part for most dielectrics, like air or glass, is very small and can be neglected. For metals, the imaginary part must be taken into account. For example, in gold, the values of the real and imaginary parts differ only by one order of magnitude in the visible and NIR regions. Figure 2.2 shows the real and imaginary parts of the dielectric function of gold. Both parts are connected by the Kramers-Kronig relation. So if one of them is known, the other can be calculated [15] [16].
The complex dielectric function consists of two major contributions. The contribution of a free electrons and a part of the interband transitions. For lower wavelengths, the dielectric function is dominated by the contribution of the interband transitions. The absorbed energy is primarily allocated into the transition of electrons between energy band of gold. For larger wavelengths, the dielectric function is described by the Drude-Sommerfeld model of the free eletron motion. In this region the electron can move freely and can be easily displaced by an external electromagnetic field [15].
In this work, the complex permittivity was calculated out of the refraction index n and extinction coefficient k based on the formulas from the book: 'Plasmonics - Fundamentals and Applications' by S. Meier. [1]

$$\epsilon_1 = n^2 - k^2 \tag{2.4}$$

$$\epsilon_2 = 2nk \tag{2.5}$$

The data for the refraction index n and the extinction coefficient k are taken from refractiveIndex.Info [17]. The following datasets are used: For gold: Olmon et al. [18] and for the glass substrate Gao et al. [19].

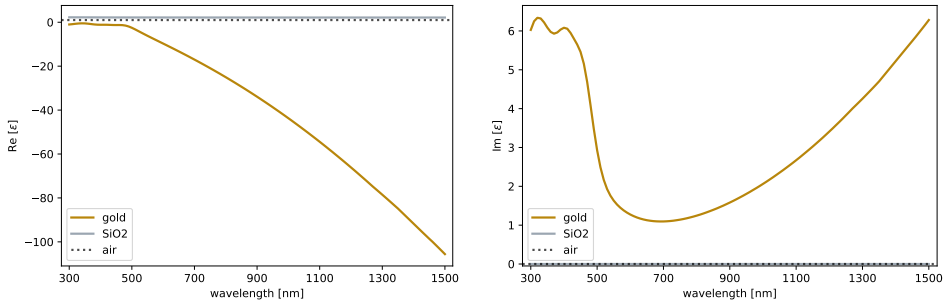

Figure 2.2: Displayed are the real **(left)** and imaginary **(right)** part of the permittivities of gold, SiO2 and air

Figure 2.2 shows the permittivities of gold, air and glass. For air, the relative permittivity of vacuum ($\epsilon_1 = 1$) is assumed because the changes in the permittivity of air are five orders of magnitude smaller than in gold. In the imaginary part of the permittivity of gold, one can see a minimum. Up to the 700 nm, the imaginary part is dominated by the interband transitions. Above this wavelength shows the part, where the contribution of the free electron movements becomes more dominant.

The dispersion relation results from the Maxwell equations, which is of further interest in the following sections, especially for the excitation of SPPs [1]. The dielectric functions of the two interface materials define the dispersion relation of a propagating SPP parallel to the interface [20].

$$k_{\mathrm{SPP}} = k_0 \sqrt{\frac{\epsilon_d \epsilon_{\mathrm{metal}}}{\epsilon_d + \epsilon_{\mathrm{metal}}}} \tag{2.6}$$

where ϵ_d and $\epsilon_{\mathrm{metal}}$ are the dielectric functions of the dielectric and the metal. Dispersion relations for the interface between air and gold and glass (SiO2) are illustrated in figure 2.3 For low k values, the dispersion relation is very similar to a photon-like ($\omega = ck$) behaviour. For larger k values, the relation starts to follow its root behaviour and approaches the surface plasma frequency

$$\omega_{\mathrm{SPP}} = \omega_P / \sqrt{1 + \epsilon_{\mathrm{d}}} \tag{2.7}$$

where $\omega_P = \sqrt{\frac{ne^2}{\epsilon_0 m^*}}$ is the plasma frequency of the metal. The plasma frequency ω_P is defined over the electron density n and charge e, the effective electron mass m^*, and the vacuum permittivity ϵ_0. For the circumstance, where air is the dielectric

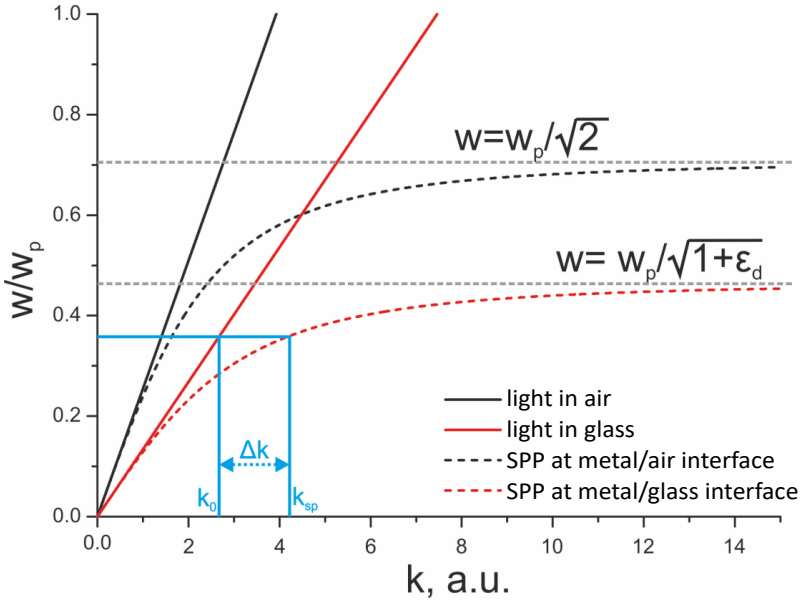

Figure 2.3: Dispersion relations of light (solid lines) and propagating surface plasmon polaritons (dashed). Additionally shown are the dispersion relations of light in air (black) and glass (red). (modified figure from [21])

$\epsilon_d = 1$, the expression 2.7 simplifies to $\omega_{\mathrm{SPP}} = \omega_P/\sqrt{2}$. [22]

The important properties, like wavelength, penetration depth and propagation length, can now be calculated from the dielectric functions and the dispersion relation of SPP. Due to the design of the sample, a thin gold triangle on glass, the following system is present: air-gold-SiO2. This system contains two dielectric/metal interfaces. At both interfaces, pSPPs can be excited. So, the following properties are calculated for the top air/gold and the bottom SiO2 interface. Especially for the penetration depth, this is very important.

2.2.1 Wavelength

With the dispersion relation from above, it is very easy to calculate the wavelength of an SPP. It is defined as follows:

$$\lambda_{\mathrm{SPP}} = \frac{2\pi}{k_{\mathrm{SPP}}} \tag{2.8}$$

The wavelength is one of the key parameters of a SPP. This property is, for example, important for the analysis of the interface materials. The group by S. Santer (University of Potsdam) uses photosensitive polymers to visualise pSPPs and can measure the material-dependent wavelength of the SPP [21] [23]. This allows conclusions to be drawn about the used materials. The further measurements revealed noteworthy interference patterns on the triangle (figure 3.8), which require closer examination in future work. This could be the interference of electric fields between the excitation light and the SPPs.
For low excitation wavelengths, the SPP wavelength shows a local maximum followed by a minimum, which can be seen in figure 2.4. The maximum results from the fact that the real part of the dielectric function of gold is less than one. The local minimum in the SPP wavelength (e.g. for SiO2/gold at 500 nm) is the point where the values of the dielectric constants are nearly equal ($\epsilon_{\mathrm{dielectric}} \approx -\epsilon_{\mathrm{metal}}$). For larger wavelengths, the SPP wavelength follows the root-like increase of the dispersion relation.

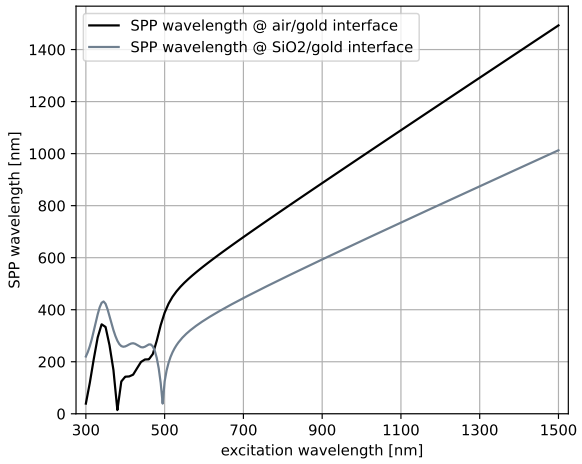

Figure 2.4: Simulation of the SPP wavelength at the interfaces air/gold (**black**) and SiO2/gold (**grey**) for variable excitation wavelengths

2.2.2 Penetration depth

As mentioned above, SPPs are excited at both interfaces of the gold layer and enter the metal from both sides. The gold layer, with its specified 20 nm, is very thin. For detailed information, see section 3.1. The electric fields of the SPPs of both sides of the metal layer start to interfere when the penetration depth is larger than the layer thickness. This results in the creation of combined plasmons with unknown properties. To prove this, the penetration depths δ_i for both interfaces are determined in both the dielectric and the gold film as follows [24]

$$\delta_i = \frac{\lambda}{2\pi} \left| \frac{\epsilon_d + \epsilon_{\text{metal}}}{-\epsilon_i} \right|^{\frac{1}{2}} \tag{2.9}$$

where i refers to the dielectric constant of either the dielectric or the metal, that is currently being observed. The following figure 2.5 shows the penetration depths for both materials at the upper (air/gold) and lower (SiO2/gold) interfaces.

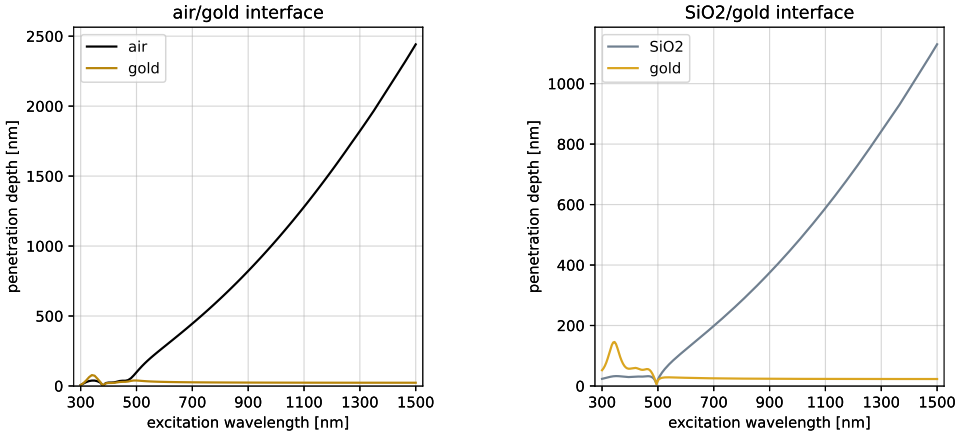

Figure 2.5: Penetration depth of the surface plasmon polariton intensity at the upper and lower interface of the sample. **Left:** Upper air/gold interface, **right:** Lower SiO2/gold interface

First, the penetration depth into the dielectric is much larger than in the metal. The electric field penetrates up to the micrometre scale into the dielectric while only reaching several nanometers in the metal. This means, that the electric field of the SPP is mainly located in the dielectric part of the interface, here air and

quartz. To gain further insights into the penetration depth into the metal from both interfaces will be examined.

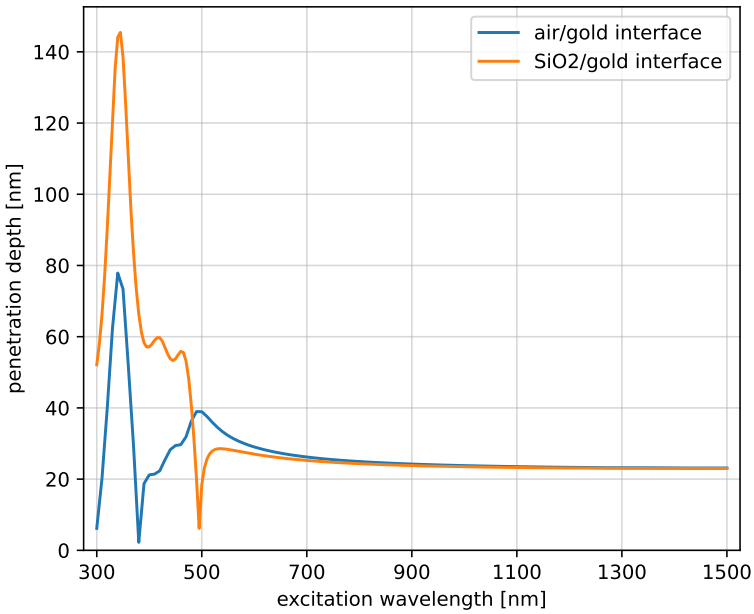

Figure 2.6: Comparison of the penetration depth of gold at both interfaces air/gold and SiO2/gold

Figure 2.6 illustrates the penetration depth into the gold layer from both interfaces.

For small excitation wavelengths, the maximum and minimum values that were previously observed in Figure 2.4 are once again evident. The underlying origin of these phenomena was addressed in the preceding section. As will be explained in greater detail in the following section, significant propagation of SPPs can only be expected at excitation wavelengths above 550 nm. Thus, the range up to 500 nm is less relevant for the investigation of the propagation behaviour. Above 500 nm, the penetration depth slowly decreases with higher excitation wavelengths. It has been established that the calculated penetration depth exceeds the specified layer thickness of the gold film. This finding suggests the presence of an interaction between the SPPs, although the nature of this interaction remains to be elucidated.

2.2.3 Propagation length

The SPPs most significant attribute for the following investigations is the propagation length L. The length of the triangle is defined as the minimum distance that an SPP must travel along the interface, as is only an SPP that propagates the distance between the base edge and the tip that can drive a reaction at that tip position or, as in the present work, couple out in the form of light and can be investigated. The propagation length can be calculated from the complex k-vector k_{SPP} of the SPP [24] [3] [25]

$$k_{SPP} = \frac{2\pi}{\lambda} \cdot \sqrt{\left(\frac{\epsilon_d \epsilon_{metal}}{\epsilon_d + \epsilon_{metal}}\right)^3} \cdot \frac{\mathrm{Im}(\epsilon_{metal})}{2\epsilon_{metal}^2} \tag{2.10}$$

$$\Rightarrow L = \frac{1}{2k_{SPP}} \tag{2.11}$$

.

The complex k-vector is utilised to incorporate the imaginary part of the dielectric function of gold into the calculation. Consequently, losses and absorption processes are considered. This results in a reduction in the intensity of the SPPs with increasing propagation distance from the excitation site. The distance at which the intensity declines to the value 1/e is designated as the propagation length L. As displayed in figure 2.7, the propagation length increases nearly exponentially with larger excitation wavelengths. For the range of 300 – 500 nm the length is very small. Here, the interband absorption of gold dominates, and no pSPPs are excited. With the decreasing influence of the interband transitions, the propagation length increases around 550 nm. This increase continues to the near-infrared region.
The shortest triangle used for this work was 30 μm long. Consequently, the minimum propagation length of 30 μm is required. So, to excite these SPPs at the air/gold interface, the excitation wavelength needs to be at least 700 nm or longer. For the SiO2/gold plasmons, a minimum wavelength of 900 nm is required.

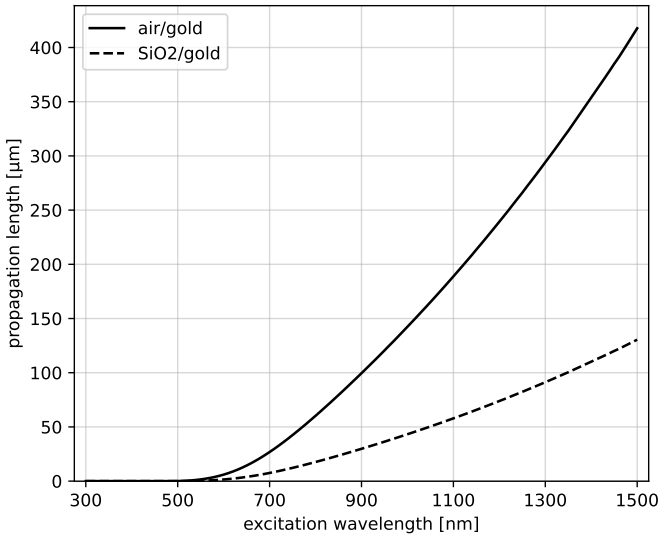

Figure 2.7: Propagation length of the SPPs at the interfaces air/gold (**solid**) and SiO2/gold (**dashed**)

2.3 Excitation of SPPs

This section provides an overview of the different excitation techniques of SPPs at a dielectric-metal interface. In general, it is not possible to excite SPPs by simple light illumination. For the successful excitation of SPPs that propagates along a dielectric/metal interface, two requirements must be fulfilled. First, the incoming EM wave needs a component of the electric field vector parallel to the interface [16] Second, the energy and momentum must be conserved between the exciting light and the SPPs. A more thorough examination of the previously mentioned dispersion relation of an SPPs parallel to the interface (figure 2.3), reveals a mismatch in momentum between the light and the SPPs. The relations between light and the SPPs don't have an intersection. As a result, an incoming photon can not couple to an SPP [24].
However, there are a lot of different methods to overcome this momentum mismatch. One of them is already illustrated in figure 2.3. By using a material with another refractive index, for example, glass, the slopes of the dispersion relations decrease. This is used in the Kretschmann- and Otto-Configuration [26] [27]. In this method, light, which propagates through a medium, can couple to SPPs at the metal/dielectric

interface with a smaller refraction index. (e.g. incoming light in glass or oil to a SPP at a metal/air interface). This creates an intersection between both dispersion relations. At this point, energy and momentum conservation are simultaneously fulfilled and an incoming photon couples to an SPP at the interface [1].
Another way to overcome the momentum mismatch is by scattering light at surface defects like edges, gratings or particles. This is the method in this work. The later specified gold triangles consist of a sharp base side, which can be seen as an edge structure. The idea is to excite SPPs at the base side and focus them on the tip. Luckily, the sharp backside is all one needs because this sharp edge provides an additional k-vector to fill in the difference between the dispersion relations. A sharp edge is an abrupt discontinuity at the surface and can be treated as a Heaviside function. The Fourier transform of the Heaviside step function is a constant distribution and covers up a broad spectrum in k-space. This provides for each incoming wavelength a suitable momentum vector Δk between the dispersion relations of light and the SPP [24] [28]. After the k-vector mismatch is resolved, the incoming photons can couple to SPPs while considering the energy conservation. This is schematically displayed in figure 2.8 case b).

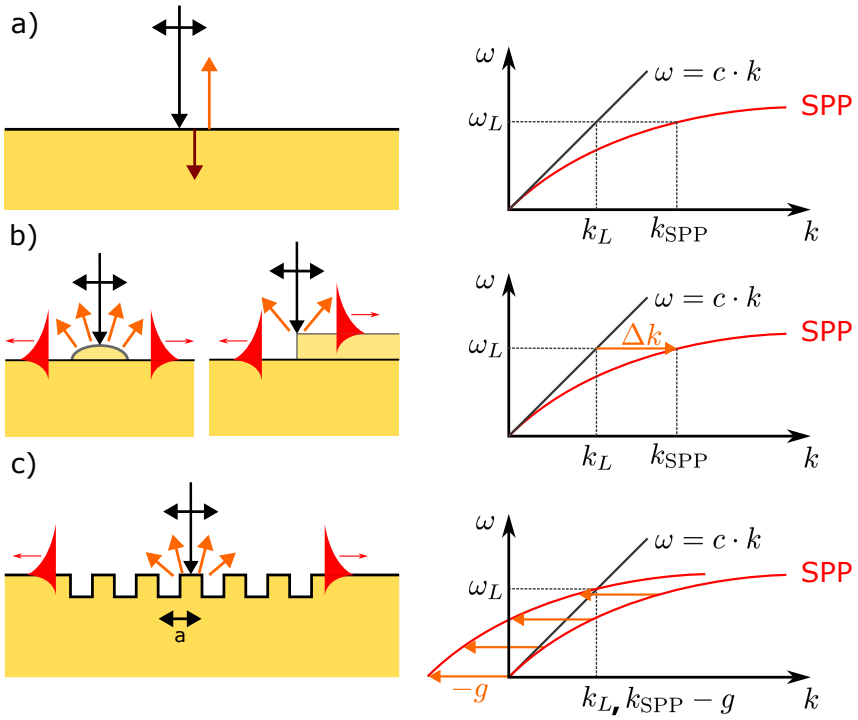

Figure 2.8: Dispersion relations of light and SPPs; a) Incoming light perpendicular to the interface don't couple to the plasmon due to the missing match in the dispersion relations. b) The excitation on surface defects or edges compensates the momentum mismatch between the dispersion relations. This provides an additional k-vector Δk. c) Grating coupling shifts the SPP dispersion relation by the reciprocal vector $-g$ and creates an intersection with the relation of light. (based on and adapted from figure of [24])

According to the calculation of the SPP wavelength, a photon doesn't excite an SPP with the same wavelength. As mentioned before, the sharp edge provides a broad range of suitable k-vectors. So, with a broad excitation spectrum, like white light, a wide range of SPPs can be excited at the triangle base.

A third method is the usage of gratings or other periodic structures, like grooves or holes, with a lattice constant a. A successful coupling between a photon and an SPP takes place, whenever the condition

$$k_{\mathrm{SPP}} = k_{\mathrm{Photon}} \sin\Theta \pm ng \tag{2.12}$$

is fulfilled. Here, Θ is the angle of incidence, n the diffraction order, and $g = \frac{2\pi}{a}$ the reciprocal lattice vector [24] [1] [29] [20].

The reciprocal lattice vector g provides an additional k-vector, which affects the dispersion relation. The sum of the plasmon momentum vector k_{SPP} and the lattice vector g results in a shift of the whole SPP dispersion relation by $\pm g$. As displayed in figure 2.8 case c), a shift of the dispersion relation by $-g$ creates an intersection between the SPP and light dispersion relation. At this intersection point, a coupling between light and SPP is possible. In comparison to sharp edge excitation, this technique is very wavelength-sensitive due to the fact that the grating provides only a small range of suitable k-vectors. This means the grating must be optimised to the excitation light or be selective to a specific range of wavelengths when using a broad excitation spectrum. Crucial parameters for the selectivity and the coupling efficiency are grating spacing, height, width, and the number of grating lines [30] [31] [32].

2.4 Coupling and transmission

The excitation of surface plasmons was described in the previous section. This was primarily concerned with the conservation of energy and momentum between light and the surface plasmons. This section derives a prediction of the expected spectrum of the light emission at the tip. Figure 2.9 illustrates a schematic representation of the composition and origin of the expected spectrum. The base side of the triangle is illuminated with the white light laser. As mentioned before, the incoming light couples to SPPs, which propagates along the air/gold interface. At the tip, the SPPs decouple /couple out in the form of light, which is analysed with the spectrometer.

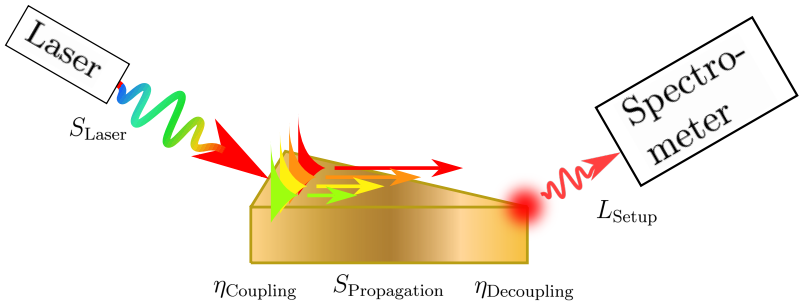

Figure 2.9: Schematic representation of the light-SPP interaction on a gold triangle. The incoming WL-light excites surface plasmons at the base side. These propagate along the air/gold interface to the tip and decouple in the form of light, which is analysed with a spectrometer

Equation 2.13 summarises the composition of the expected spectrum of the light emission at the tip when the triangle base is excited with a laser. [33].

$$S_{\text{tip}} = S_{\text{Laser}}\, \eta_{\text{Coupling}}\, S_{\text{Propagation}}\, \eta_{\text{Decoupling}}\, L_{\text{Setup}} \tag{2.13}$$

where

- S_{Laser}: excitation spectrum
- η_{Coupling}: coupling efficiency from light to SPP at the triangle base side
- $S_{\text{Propagation}}$: wavelength-dependent propagation length along the triangle
- $\eta_{\text{Decoupling}}$: decoupling efficiency from SPP to light at triangle tip
- L_{Setup}: influence of the setup, e.g. losses and detector sensitivities

In the following, the individual components are analysed in more detail. In one regard, some components can be determined experimentally. In contrast, only theoretical estimates and assumptions could be made for others. First of all, the propagation behaviour $S_{\text{Propagation}}$ along the triangle is the propagation length of the SPPs. This was already mentioned earlier in section 2.2.3. For this the simulation predicts an exponential-like increase of the propagation length for increasing excitation wavelengths. The excitation S_{Laser} and the experimental setup L_{Setup} are described in chapter 3, but a quantitative statement about their influence will be discussed in chapter 4.
The following sections will discuss the two remaining components. The coupling efficiency at the base side and the decoupling at the tip of the triangle.

2.4.1 Coupling at the base side

This section discusses the coupling efficiency (CE, η_{Coupling}) between the incoming light and the excited surface plasmon polariton at a sharp edge structure like the base side of the triangles. As mentioned previously, this is, together with the decoupling efficiency, a crucial component in predicting the propagation behavior of the SPPs along the triangle. Unfortunately, the theory for the present system has not yet been worked out sufficiently, that only assumptions based on similar work can be made here. The paper by Cruz et al. [34] discusses the coupling efficiencies at different types of discontinuities like steps or groves.

The values in this paper don't match the parameters used in this work, but they give a better understanding of the key coupling parameters, such as wavelength, step height, and angle of incidence.
The group calculated the CE for a gold step structure for three different excitation wavelengths (633 nm, 750 nm and 980 nm) as a function of the step height.

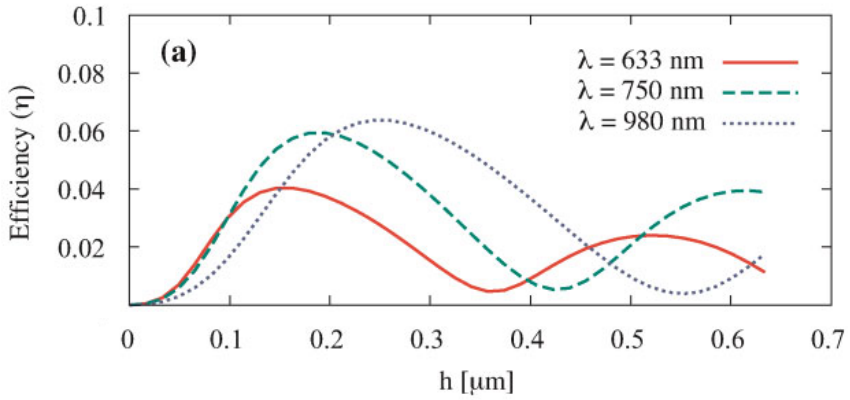

Figure 2.10: Coupling efficiency for a gold step structure. Displayed is the CE as a function of the step height for the excitation wavelengths 633 nm, 750 nm and 980 nm. Angle of incidence is 30° from the sample normal [34].

Concerning the simulation of the propagation length (sec. 2.2.3), which increases from 550 nm, these wavelengths provide a good selection of the white light spectrum that will later be used. In general, this simulation shows that different excitation wavelengths have different coupling efficiencies at the same step height. For example, the CE maximum of 633 nm is 4% at a height of around 0.15 μm. On the other hand, for an excitation wavelength of 980 nm, the maximum is 6% at a height of 0.3 μm and follows a flatter slope. So, one can see a clear dependency between the coupling efficiency as a function of the excitation wavelength and the step height of the edge. For this work, the region of interest (ROI) is around 0.025 μm due to the gold layer height of the triangle. For more details on the layer height, see the following chapter 3.1. In this ROI the coupling efficiencies are very small and close together. Unfortunately, this graph shows the coupling efficiency primarily for step heights in the hundreds of micrometer regime. So, only an estimation for the CE at a step height of around 25 nm can be made. First, the coupling efficiencies for all three wavelengths are below 1%. At a closer look at this ROI, one can see that the 633 nm line (solid red) is slightly above the 750 nm (dashed green) course.

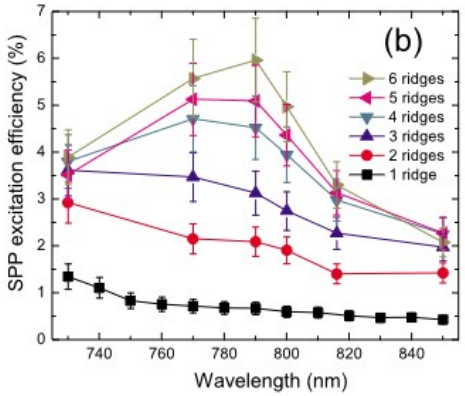

Figure 2.11: Coupling efficiency as a function of the excitation wavelength for a different number of 50 nm high and 150 nm wide gold ridges. The black squared curve (1 ridge) shows a low decrease in efficiency for higher excitation wavelengths [30].

And both of them lie significantly above the NIR excitation light (980 nm, dotted blue). This means the coupling efficiency decreases from the visible to the near-infrared region.
The area above 700 nm is covered by the work of Radko et al. [30]. They study the CE at gold nanoridges (50 nm in height and 150 nm wide). The coupling efficiency for one ridge provides the closest approximation to the edge structure used in this work. Figure 2.11 shows the SPP excitation for a different number of ridges as a function of the excitation wavelength from 730 nm to 850 nm. It predicts a slight decrease in coupling efficiency for larger wavelengths (black squared line). This is consistent with the calculations from La Cruz et al. For this work, the following assumptions for the coupling efficiency from a photon to an SPP at the base side of the triangle will be made. First, the efficiency is probably below 1% for each excitation wavelength. And second, it decreases for higher wavelengths.

2.4.2 Decoupling at tip

This section will examine the decoupling efficiency (DE, $\eta_{\text{Decoupling}}$) of the SPPs at the triangle tip. As mentioned before, there is a momentum mismatch between light and SPP dispersion relations. This means the SPPs can not couple out during their propagation along the interface. SPP scattering at discontinuities at the interface provides additional k-vectors, which can compensate the mismatch between the dispersion relations. As before, the edge of the tip can be seen as a sharp discontinuity, which creates a broad variety of k-vectors. So, a suitable k vector is available for each SPP with a propagation length equal to or larger than the triangle length to decouple at the tip in the form of light [35] [36].

There has been no research conducted on the wavelength-dependent pSPP-based light emission at a sharp edge of a thin gold film. This will result in an assumption being made based on similar or related works and previously gained knowledge.

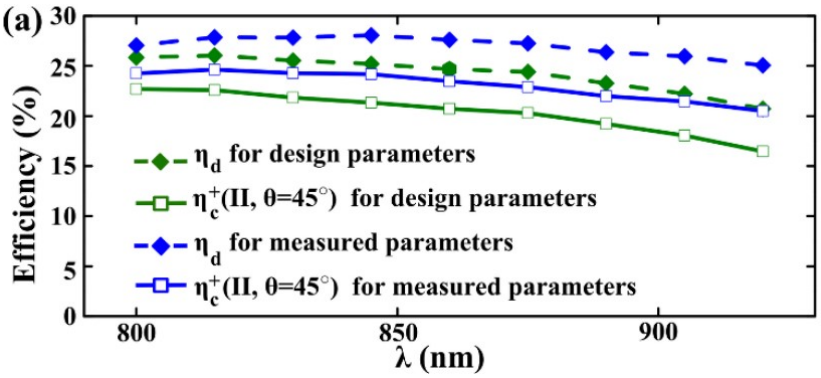

Figure 2.12: Simulated (green dashed) and measured (blue dashed) coupling and decoupling efficiency [33]

Figure 2.12 shows the calculated and measured decoupling efficiency (DE) for the NIR spectrum of a gold grating. The DE shows an estimated maximum slightly above 800 nm and a low decrease in efficiency to larger wavelengths. The same goes for wavelengths below 800 nm, where course also indicates a decreasing behavior. [33]
In the following assumption, the grating is reduced to a single ridge, and the previously mentioned influences of the grid parameters are combined. This results in the following conclusion: the general DE over the entire spectral range decreases. This was also seen by the coupling efficiency, where the efficiency drops with the number of ridges in the grating. Furthermore, it was seen that the number of ridges

creates a shift in the maximum location. So, with fewer ridges in the grating, see a small maximum and probably shift to a smaller wavelength. Overall, for the decoupling at the tip, it is assumed that the efficiency is very low and is slowly decreasing for higher SPP wavelengths. As the coupling efficiency, this should lead to a flatter slope in the light emission for a higher wavelength. But this has to be checked experimentally or via simulations.

The following brief summary outlines the anticipated light emission at the triangle tip. The light is the result of the interaction of five distinct subsystems, as previously outlined. The components excitation light and setup will be determined and discussed in forthcoming chapters through experimental means. However, estimates could be made for the interaction of light and surface plasmon at the base and tip, which appear to demonstrate a decline in coupling and decoupling efficiencies towards the near-infrared spectrum. The calculation of the propagation length indicates an exponential increase in light intensity at higher wavelengths. This is due to the enhancement of coupling efficiencies, which results in a flatter increase or flattening out in the NIR spectrum.

3 Methods

The main goal is to build a setup to excite and observe pSPPs on gold nano triangles. So this section describes all the different approaches and experimental methods to excite and observe SPPs. The basic idea is to excite SPPs at the base side of a gold triangle. The SPP then propagates along the interface to the tip, where the triangular shape focuses them. For this, the first section describes the sample with the gold triangles. Additionally, the specified properties of one of the most used triangles are checked. The second part illustrates the different setups and expansions that are required for the experimental approaches. It started with simple laser excitation and a camera image and went up to a grazing incidence white light excitation with two highly sensitive spectrometer detectors.

3.1 Sample

First, a brief description of the sample is required. Gold triangles of different dimensions are lithographed on a microscopy slide (soda–lime glass). The sample was created by Bikash Das Mohapatra from the workgroup of Georg Schmidt [37].

The triangles are organised in patterns with two different compositions. All dimensions vary in the first pattern, while the length is kept constant in the other. Pattern 1 contains a lot of triangles with different lengths (70 μm, 50 μm and 30 μm) and base widths from 4 μm up to 16 μm. A thickness of around 20 nm is specified for all triangles. Figure 3.1 displays a schematic representation of the arrangement of pattern 1. Each triangle is named by its position on the sample for better identification. So, every triangle is given a unique name: pattern, column and row.

The triangle sample is analysed using an atomic force microscope (AFM) to verify the manufacturer's triangle specifications. Figure 3.2 shows the image of a triangle, which is 50 μm long and has a base width of 16 μm. A general inspection of the condition and length of the triangle is conducted. Subsequent investigations, shown in figure 3.3 are initiated on the triangle's base and tip. These measurements are utilised to verify other properties of the triangle, including the width of the base side and tip, as well as the layer thickness.

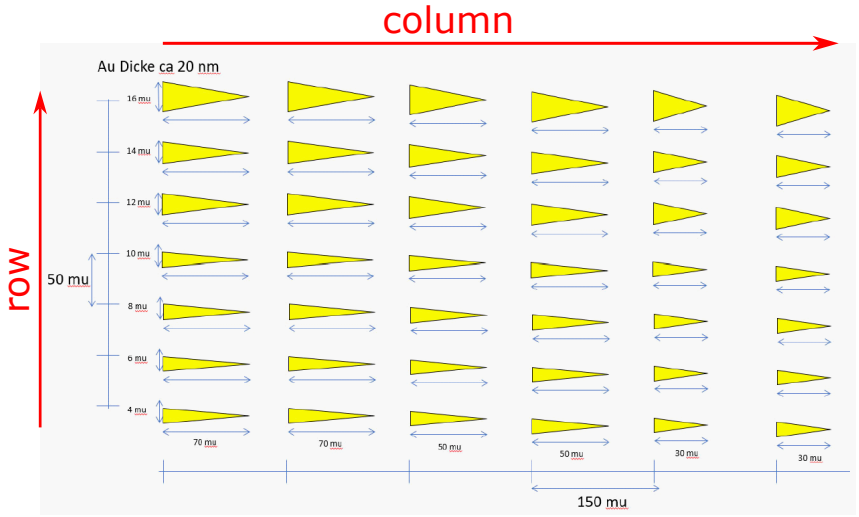

Figure 3.1: Dimensional properties of the triangles in design pattern 1. Additionally, the nomenclature of the individual triangles is shown. First: **pattern**, then from the left to the right: **column** from 1 to 6 and from the bottom to the top: **row** from 1 to 7

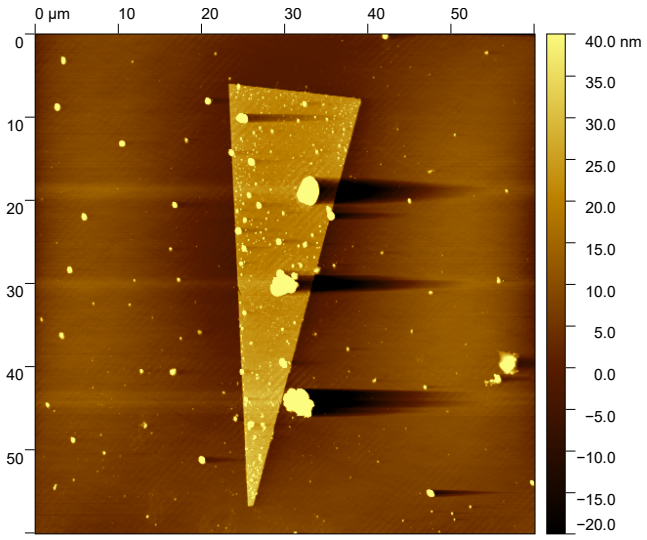

Figure 3.2: AFM Image (Digitally reworked with Gwyddion) of a triangle with the dimensions: length: 50 μm and base width: 16 μm

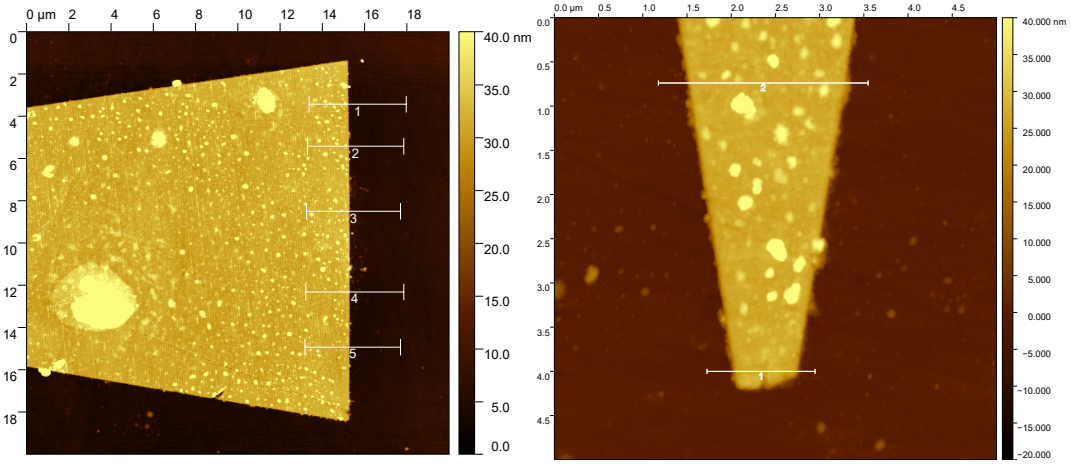

(a) Base side **(b)** Tip

Figure 3.3: AFM Image (Digitally reworked with Gwyddion) of the base side (**left**) and tip (**right**) of triangle displayed in figure 3.2

Along the different cross sections Gwyddion provides the following triangle properties:

property	specified	measured
length	50 μm	50.63 μm
width base side	16 μm	16.46 μm
width tip	20 nm	850 μm
gold layer thickness	20 nm	$\sim$ 27 nm

Table 3.1: Comparison of the measured properties of a triangle (length: 50 μm, width base side: 16 μm) obtained with AFM and Gwyddion to the specified data from the producer

The majority of the measured triangle properties correspond to the data specified by the producer. Only the measured tip width of 850 nm differs a lot from the specified 20 nm. The tip may be broken off due to the frequent use of the sample. A thorough examination of the three images (fig. 3.2 and 3.3) reveals the presence of numerous bright spots, which are indicative of dirt particles that have accumulated over time. Cleaning processes like organic solvents or UV-ozone cleaning only removed a small amount of the dirt from the sample. Further analysis of additional triangles reveals analogous signs of wear and tear.

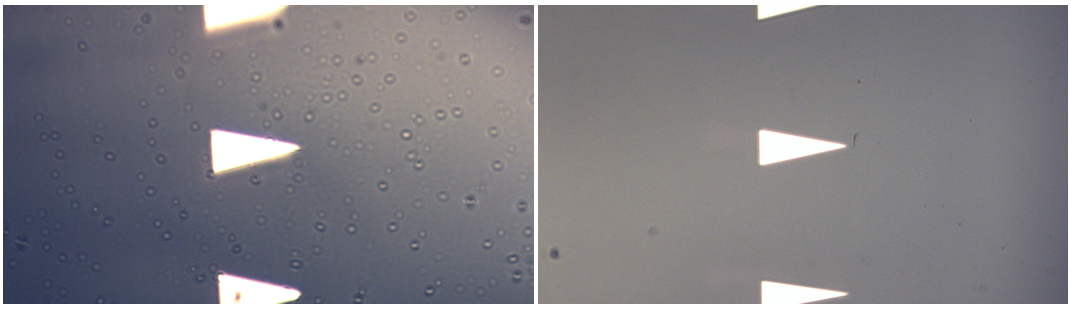

Figure 3.4: Left: Camera image before cleaning and adjustment. The triangle in the field of view is blurry and overlapped with a lot of dirt particles **Right:** Camera image after cleaning the optical elements and adjusting the camera focus. A clear and sharp triangle can be seen

3.2 Setup Versions

The basic setup is a self-made Raman microscope from the UDKM Group of Matias Bargheer [15]. This setup offers a good framework for the observation and the excitation of pSPPs. The basic setup is the same for all variants. It consists of an illuminating lamp, a CMOS camera, an objective, and a movable stage. Figure 3.5 shows a schematic representation of the basic setup and the needed components. This setup enables two main functions. From one perspective, it provides full control over the sample thanks to the movable stage in the x-y plane. From another perspective, the triangles are illuminated and observed using the lamp and the CMOS camera.
The first image of a triangle with this basic microscope shows two problems. First, the camera is out of focus, and second, the image is very dirty. The left image of figure 3.4 displays a very blurred triangle and a lot of dirt particles distributed over the whole image. With this state of the setup, it is difficult to see details, and the dirt particles on the camera overlap with important ROIs like the tip or base side of the triangle. This distorted the subsequent measurements. So, the first step is to clean all optical elements and readjust the camera focus. The right image of figure 3.4 shows a clean and sharp camera image of the triangle.
Having established the fundamental framework for triangle selection and achieved precise observation, the subsequent focus will be on the excitation of SPPs within the delineated triangle.

3.2.1 V1: Perpendicular Excitation

The initial approach was a simple perpendicular illumination of the sample. This method is founded upon the SPP excitation from previous works undertaken by, for instance, the Santer research group. They excite SPPs by perpendicular illumination of a groove in a silver film. [21] [23] In order to adopt this approach for the present work, a laser is coupled into the microscope by a suitable beamsplitter and focused at the base side of a gold nanotriangle. A white light laser (WL, NKT photonics SuperK extreme FIU-15) is used as the laser source, as this provides a broad spectrum of wavelengths from 400 up to 2400 nm. According to the theory, excitation wavelengths of at least 600 nm, preferably 750 nm, are required to ensure effective propagation lengths of SPPs. The built-in CMOS camera of the microscope is used as the detector. Figure 3.5 shows the fundamental setup, as previously outlined, and the perpendicular excitation with the white light laser.

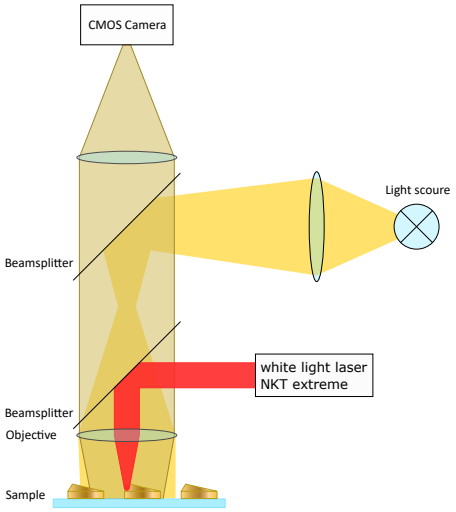

Figure 3.5: Basic setup: A movable sample holder in the x-y plane. Above the sample is a height-adjustable objective. A light source and a CMOS camera are used as illumination and imaging devices. The white light laser is coupled in the pathway by a beamsplitter and illuminates the triangle base perpendicular from the top

As illustrated in figure 3.6 (a), the image captured via the top-mounted CMOS camera demonstrates the perpendicular laser excitation of the base side of a triangle without illuminating the sample. Only a bright spot can be seen. The resultant image is a bright spot, as depicted. The image on the right (b) displays the cross-section through the bright spot. The images illustrate the saturation of the CMOS

(a) Dark image of the laser spot on the triangle base

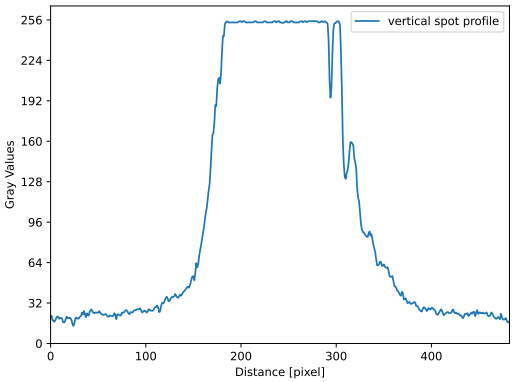

(b) Vertical profile through the laser spot shows already by a low laser intensity a saturation of the camera

Figure 3.6: Saturation effect of the CMOS camera chip by perpendicular white light excitation of the triangle base

detector by the reflected excitation light that is transmitted by the beamsplitter. Notably, this phenomenon occurs even at low laser powers of 20%, despite the high reflectivity of the beamsplitter (R 90: T10). The objective is to observe a light emission at the tip; however, this excitation method merely reveals the bright spot of the saturation.

3.2.2 V2: Exciation under grazing incidence

In order to overcome the saturation problem, a change is made to the excitation method. The setup is expanded by incorporating a grazing incidence (GI) path, where the exciting light is directed towards the base of the triangle at a sharp angle, see fig. 3.7. The key advantage of this method is that the incidence light is reflected away from the objective, according to the law of reflection. Consequently, the excitation light is prevented from reaching the detector. Instead, only the scattered and emitted light from the sample is collected by the objective and reaches the camera. A disadvantage of this method is the limitation of the angle of incidence (AOI). The AOI is limited by the distance between the sample and the objective, also called working distance. In this setup, the objective has a working distance of 1 mm. The maximum possible angle without the incident light hitting the housing of the objective is 18°. Since only the perpendicular component of the wave vector can excite SPPs, the steep AOI results in a loss of excitation power due to the decomposition of the incoming electric field vector. Under this AOI, the effective

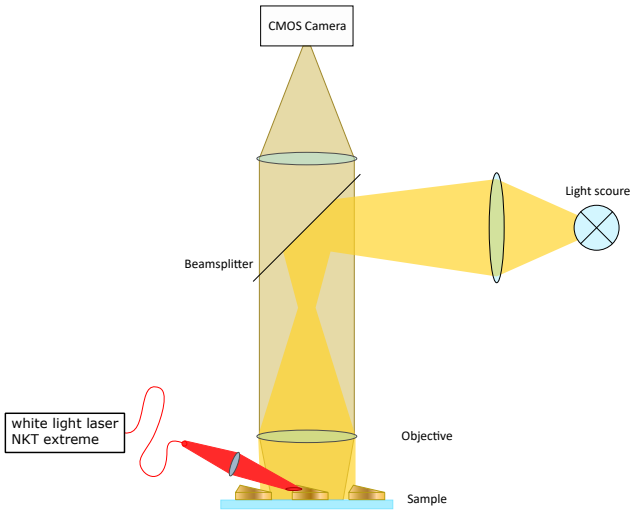

Figure 3.7: Grazing Incidence Setup for the white light excitation from the side

excitation power decreases to 30%. In addition to the vector decomposition, another effect decreases the excitation efficiency of the SPPs: due to the sharp angle of incidence, the laser spot becomes larger and adopts an elliptical shape with respect to the sample plane. This results in a reduction of the available amount of light at the base side.
The top image of figure 3.8 depicts an illuminated triangle. It has a total length of 50 μm and a base width of 16 μm. As displayed in the figure 3.7 above, the grazing incidence excitation via white light originates from the left side, with the laser focused on the base of the triangle. In accordance with theoretical predictions, the sharp edge provides a suitable k-vector for each wavelength of the WL-spectrum to overcome the momentum mismatch in the dispersion relations between light and SPP. Thus, a photon of each wavelength can couple to a SPP at the edge. Subsequently, the SPPs propagate along the surface towards the tip, where they couple out in the form of light, which can be detected with the CMOS camera of the microscope.
A closer inspection of the tip reveals a faint glow at its position, with the emitted light tending to be in the red spectral range. The effect is more clearly visible when the background lighting is switched off, as demonstrated in the bottom part of figure 3.8. At the highlighted triangle tip a red light is clearly visible. A significant spectral difference is observed between red light at the tip and the WL excitation at the base side. The calculations above predict a greater propagation length for SPPs with longer excitation wavelengths. Consequently, the predominantly red

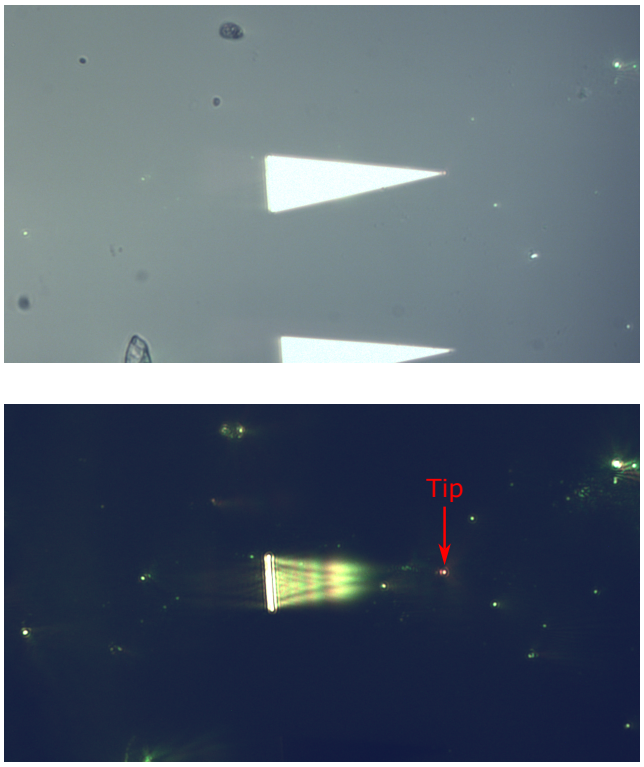

Figure 3.8: Triangle with a total length of 50 μm and a base width of 16 μm. The base side is excited with white light under grazing incidence. **Top:** Background illumination is switched on. A weak red light can be observed at the tip. **Bottom:** Background illumination is switched off. The tips position is highlighted. The red light emission is more clearly visible. Furthermore, an interference pattern extending from the base side is revealed.

light at the tip serves as a reliable indicator that the emission is generated by outcoupling pSPPs. Furthermore, the dark image shows an interesting interference pattern expanding away from the base side. Explaining this pattern's origin and behaviour will be part of future investigations. In contrast to the perpendicular WL excitation of the triangle, a red-centered emission can be observed at the tip as a result of the white light excitation under grazing incidence. However, because the top-mounted CMOS camera only resolves intensity, some workarounds are required to gain further information on the observed emission. To aquire a polarisation- and wavelength-dependent resolution of the light at the tip, both parameters are varied in following measurements. The polarisation of the incoming light can be controlled with a linear polariser from 0° to 180°. 0° denotes a perpendicular-

and 90° a parallel orientation of the electric field vector to the base side of the sample plane. The spectral range of the incidence light can be selected from the WL laser with the corresponding NKT monochromator. It operates is the range from 420 to 840 nm with a minimum bandwidth of 10 nm, allowing for spectrally resolved measurements of the light at the tip regarding the incident light. For both variations, the same integration method is used. For all polarisation- or wavelength steps, an image is taken with the CMOS camera. The image stack is analysed using Python: In the first step, a region of interest is defined around the tip position for the entire image stack, so the same region is analysed in every image. The intensity values in the ROI are integrated into both dimensions. The obtained scalar is then background-corrected with a second ROI of the same size [38]. The second ROI is far from the triangle and other scattering features. Finally, the data are normalised with the measured power for each step.

3.2.3 V3: Final setup

Even with the previously outlined changes, the setup is very limited in its application. A spectral resolution of the tip light is only possible with a workaround. In addition, the CMOS camera is not very sensitive and has a built-in IR short-pass filter, with a cut-off wavelength at around 650 nm, see figure 6.1 in the Appendix. Another limiting factor is the monochromator. Its upper limit of 840 nm does not reach far enough into the NIR, where the interesting SPPs are exited. To circumvent these problems, a highly sensitive spectrometer (Andor Kymera 328i) was added to the setup. Two high-resolution cameras are connected to the spectrometer. The Andor iXon Ultra 897 camera is used for high-resolution images of the triangle, while the Andor Newton 971 EMCCD camera is used to take a spectrum of the weak light emission at the tip position.

However, the newly acquired spectral resolution comes at the expense of spacial resolution which is completely lost. Another disadvantage is that the recorded recorded spectrum would not only contain the light from the tip but also the scattered light from the base side and particles distributed on the sample. Consequently, it would not be possible to accurately determine the spectrum originating from the light at the tip based on the recorded spectrum. Furthermore, the surrounding scattered light is significantly more intense than the light emission at the tip.

To recover the spatial resolution, a confocal spatial selector was implemented to physically select the ROI. The spatial selector is consists of two lenses and a pinhole. The lenses both have the same focal length and are twice the focal length apart. The first lens projects an image of the sample region onto the pinhole slide with a 20x magnification. It only lets light pass, that originates from a certain ROI.

The second lens is then utilised to collimate the light rays once more, staying true to the original beam diameter. In this setup, a pinhole with a diameter of 100 μm is used. Given the 20x magnification, the pinhole selects a circular ROI of 5 μm on the sample. To test the functionality of the pinhole, so whether it selects the desired ROI or not, the triangle tip is illuminated with an additional laser (Coherent 488 nm). The pinhole is then placed on the illuminated position so that the laser should be clearly visible in the spectrometer.

Prove of concept can be found in the left image of figure 3.9. The depicted spectrum shows a highly intense laser peak at around 488 nm. The second image on the **right** of figure 3.9 shows the spectrum after moving the pinhole away from the tip position until no more significant laser signal was visible. The final position of the pinhole is around 3 pixels next to its origin location from the **left** image. Under consideration of the detectors pixel size (16 μm $\times$ 16 μm) and the magnification (20x), the ROI was moved 25 μm away from the spot illuminated by the 488 nm laser. The negative values in the spectrum from 400 – 700 nm occur due to the background correction of the measurement.

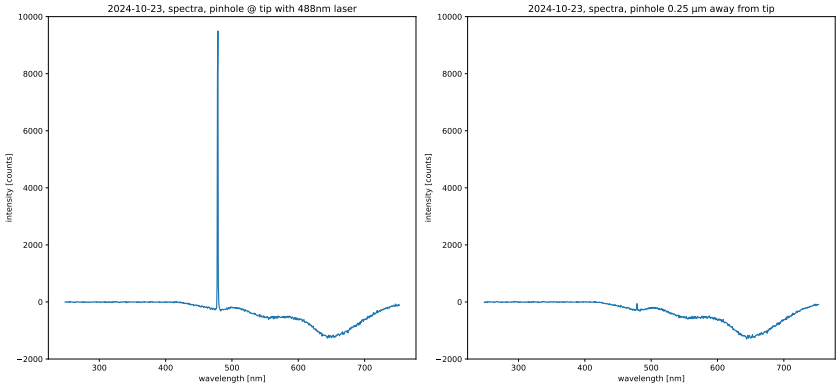

Figure 3.9: Spectra measured with the Andor spectrometer to prove whether the detector sees the ROI or not. The tip of a triangle was illuminated with a 488 nm laser. **left:** The ROI created by the pinhole is at the illuminated position. The spectrum shows a highly intense peak at 488 nm.**right:** The pinhole was moved until no significant signal was visible. The final position was 25 μm away from the illuminated tip position.

This confirms that the detector (here: Newton EMCCD at the spectrometer) only sees the region of interest created by the pinhole. The restoration of spacial information is very helpful as only the emitted light from the tip is supposed to be analysed in the following.
The calculations in section 2.2.3 predict larger propagation lengths in the near-

infrared (NIR) regime. The original setup is designed and optimised for Raman measurements in the visible region. For example, dielectric mirrors are installed for this purpose. These are optimised for the visible range up to 800 nm. Beyond this, their reflectivity decreases significantly. To extend the measurable region into the NIR, a second pathway is built and tested. This pathway contains NIR-optimised optical components such as silver mirrors. The pathways split above the objective via an exchangeable beam splitter and leads to an optical fiber. This can be plugged into several spectrometers. In order to test the NIR-path, both an Avantes IR and an Avantes VIS spectrometer are used as the detector unit. Unfortunately, the Avantes IR spectrometer is not sensitive enough to detect the small amount of light, which is emitted at the tip. For short integration times, the spectrometer exhibits a poor signal-to-noise ratio (S/N), so that no signal can be identified. For longer exposure times the spectrometer is saturated by the noise. The VIS Avantes spectrometer shows similar sensitivities. However in test measurements it is possible to see a spectrum of the illumination lamp with a small intensity and a poor S/N-ratio.
After the discovery, that the Avantes spectrometers are not sensitive enough to measure the light intensity at the tip properly, the optical fiber of the IR path is redirected to the Andor spectrometer (Andor Kymera 328i with a Andor Newton 971 EMCCD camera). Although this spectrometer is optimised for the visible range, it is significantly more sensitive than the Avantes spectrometer. The sensitivity information is displayed in figure 6.4 of the Appendix.
Settling on the Andor spectrometer now raises the question of whether the IR-optimised path is a viable improvement if the detectable spectral range is limited to the visible region. To decide on the best option, the intensities of a scattering spectrum from the same sample are measured with both pathways. Figure 3.10 shows the results.

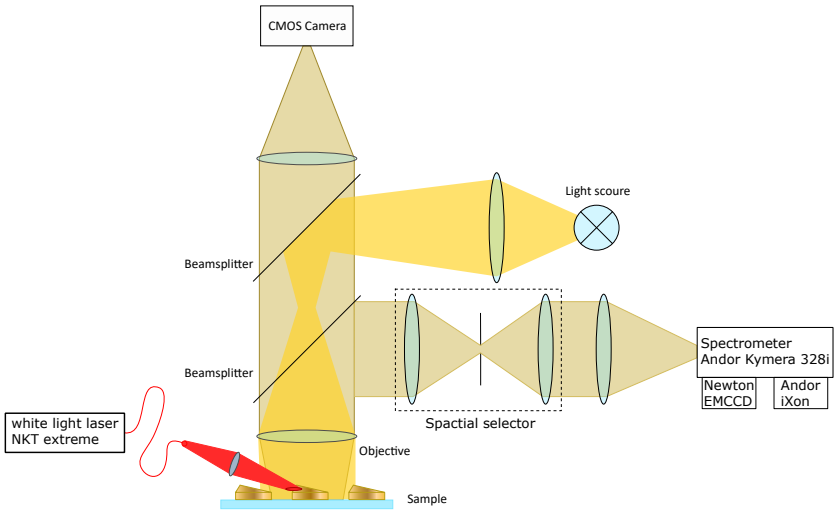

Figure 3.11: Final setup with a grazing incidence white light excitation, a spatial selector to physically select a ROI of the sample and two highly sensitive detector units. A spectrometer and a camera

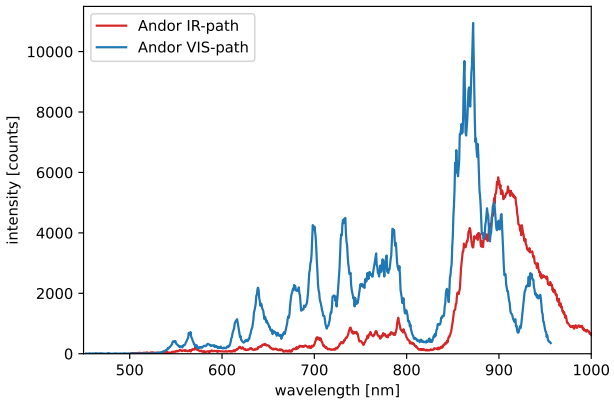

Figure 3.10: Scattering spectra of GI-illuminated gold-nanoflowers measured with the Andor Kymera spectrometer using the visible (VIS) and the near-infrared-optimised (IR) path

As expected, the spectrum of the VIS-pathway shows a much higher intensity in the VIS region than the one from the NIR-pathway. The reduced losses in the IR path do not couteract the reduced spectrometer sensitivity in the NIR region. Therefore, the path is no longer used. To summarise the final setup, which is used for the measurements in the following section. The setup is displayed in figure

3.11. The sample with the gold triangles is placed on a movable sample holder. In combination with the light source and a top mounted camera, every triangle of the sample can be moved into the field of view and observed. The base side is illuminated with a white light laser under grazing incidence. The scattered and emitted light is collected with the objective and follows the VIS optimised pathway to the Andor spectrometer. It can be selected between two highly sensitive imaging devices: A camera optimised for imaging (Andor iXon) and a camera optimised for spectral resolution (Andor Newton). Lastly the optical pathway contains a functional spatial selector to select a ROI, like the tip or base side position of the triangle.

4 Measurements and Results

Following the presentation of the theory and the experimental setup in the preceding chapters, this subsequent chapter will examine the experimental results. The objective of this examination is to study light extraction at the tip, as illustrated in Figure 3.8, to verify whether this is a plasmon-based emission. To achieve this, the setup described in the previous chapter is utilised to obtain a detailed analysis of the tip light. To ensure the accuracy of the results, it is essential to note that the measured tip light is influenced by the five subcomponents discussed in section 2.4. The influence of the different components is analysed and discussed in the various approaches.
The first sections of this chapter present the results obtained with the CMOS camera 3.2.2. The intensity of the light emitted at the tip is examined as a function both of the polarisation and wavelength of the excitation light. The second part discusses the spectral analysis of the tip light more closely. By measuring the excitation spectrum directly and taking into account the influence of the setup, a more accurate comparison can be made between the measured spectrum and the theoretical prediction.

4.1 Polarisation dependence

The first proof, whether the light emission is plasmon-based or not, is to investigate the dependence between the light intensity at the tip and the polarisation of the incoming light. As discussed in the theory section 2.3, the alignment of the electric field vector of light is important for the successful excitation of SPPs. This alignment must be both perpendicular to the edge of the triangle and parallel to the interface [24] [23].

To prove this, the setup described in section 3.2.2 extended by the linear polariser is used. The intensity of the tip light was measured as a function of the polarisation in relation to the alignment to the base edge. A polarisation of 0° or 180° means a perpendicular polarisation with respect to the triangle base. A rotation of the polariser by 90° leads to a parallel polarisation of the light about the triangle base. Figure 4.1 shows the images, captured with the top-mounted CMOS camera, of a perpendicular and a parallel excitation of the triangle base.

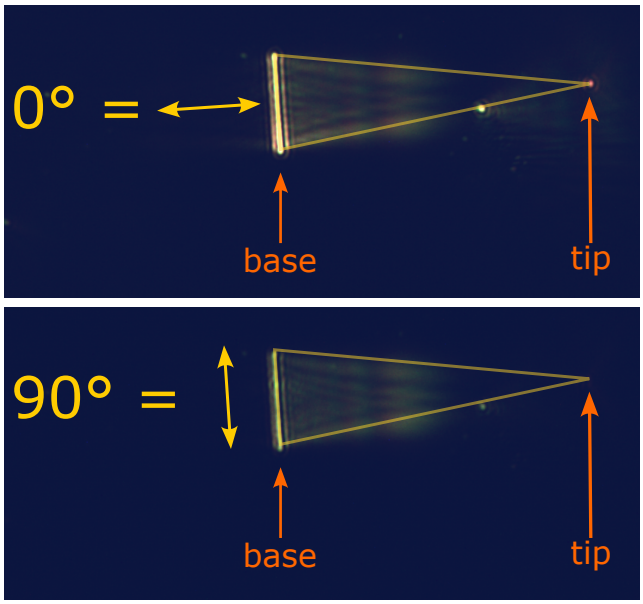

Figure 4.1: Polarisation dependent excitation of a triangle. Marked are the triangle shape, position of the base and tip, and the polarisation 0° & 90°. **top:** Polarisation 0°, a perpendicular polarisation leads to a red light emission at the position of the triangle tip; **bottom:** A parallel orientation of the electric field vector doesn't show a light at the tip.

For a perpendicular excitation, a clear red light spot can be seen at the tip position of the triangle. This light is absent for a parallel orientation of the incoming light. This fits the theory and similar works in that an electric field vector perpendicular to the triangle base is needed to excite SPP at the air-gold interface [24] [23].

A more detailed analysis of the polarisation dependence is done. Even though no significant propagation length is expected below 700 nm according to the calculations in sec. 2.2.3, the excitation wavelength is set to 610 nm with the corresponding NKT monochromator. Counterintuitively, this measurement can still be expected to yield results because the detector intensity peaks at 610 nm. This means an amplitude of even less than 1/e (defined propagation length) can be detected when it reaches the tip. As figure 4.3 shows, a light spot can be observed at the position of the tip for excitation wavelengths below 700 nm. An additional reason to use this excitation wavelength is caused by setup restrictions: the camera's built-in short pass filter prevents the use of an excitation wavelength above 650 nm. See figure 6.1 in the Appendix.

For the measurement, the polarisation is changed in steps of 10° between 0° and 180°. The ROI was as described in section 3.2.2. Figure 4.2 displays the background-corrected and normalised polarisation dependence of the light intensity at the tip.

The polarisation is changed in steps of 10° between 0° and 180°. The ROI is defined as described in section 3.2.2.

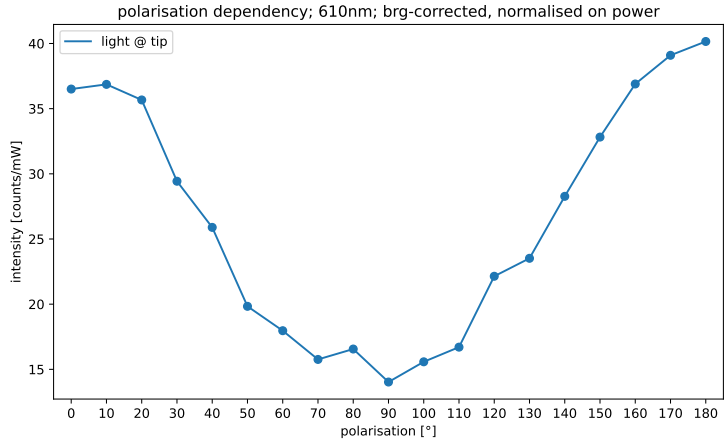

Figure 4.2: Polarisation dependence between the incoming light and tip intensity between 0° and 180°. The data are background corrected and normalised on the power of the incoming light. A clear intensity minimum is visible for a polarisation of 90° (parallel polarisation). The intensity increases towards 0° and 180° (perpendicular polarisation).

The data show a clear intensity minimum for a polarisation of 90°. For this parallel orientation, the projection of the electric field vector is parallel to the triangle base. Going up to 0° or 180°, an increase in light intensity can be observed. This means the electric field vector of the excitation light has a projection in the sample plane greater than zero. So, a coupling between the light and an SPP is possible. The maximal coupling efficiency lies at 0° or 180° when the projection of the electric field vector stands perfectly perpendicular to the base.
These observations confirm the theory that the incoming light needs a perpendicular component with respect to the triangle base to couple to a plasmon. So, for the following measurements, a linear perpendicular polarisation of the excitation light is chosen to achieve the maximal possible coupling efficiency between the incoming light and an SPP.

4.2 Wavelength dependency

The next approach is to analyse the dependence between the wavelength of the incoming light and the intensity of the emitted light at the tip. As in the previous section, the measurements are conducted with the setup using the CMOS camera

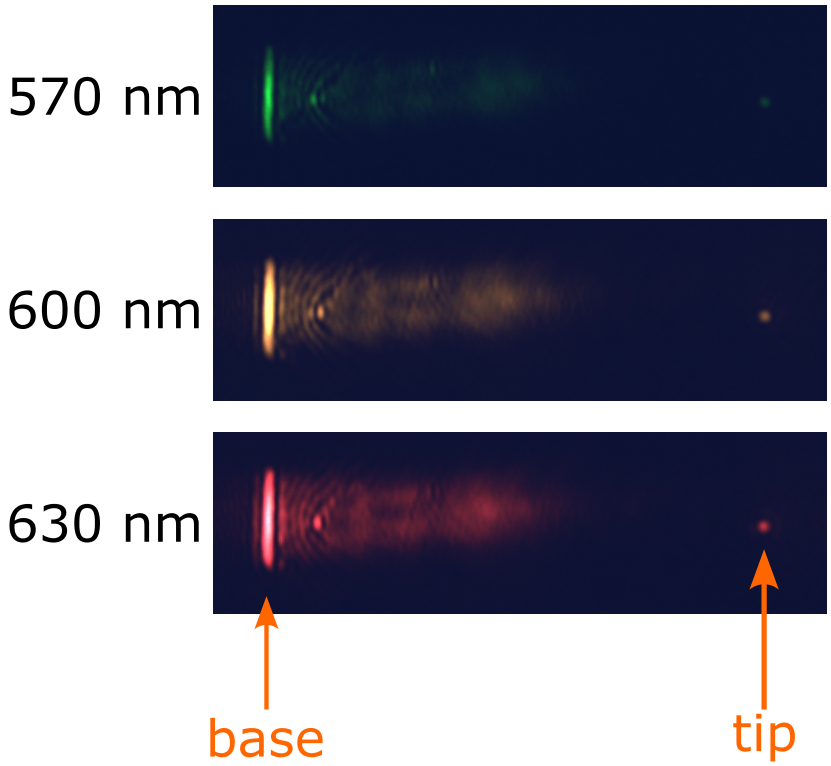

Figure 4.3: The base side of the triangle (length: 50 μm, base side width: 16 μm) is excited with different wavelengths: 570 nm, 600 nm and 630 nm. At the position of the tip, a light spot can be seen with the same color as the base side.

3.2.2, but instead of the polarisation, the wavelength is varied. Figure 4.3 depicts the captured images of the same triangle (length: 50 μm, base side width: 16 μm), but the base side is illuminated with different excitation wavelengths. First of all, the positions of the base side and the tip are clearly visible. Surprisingly, the tip shows the same colour as the base side for all three wavelengths. According to the simulation of the propagation length, it's very unlikely that the observed lights at the tip position are plasmon-based emissions. The simulation predicts that an excitation wavelength of at least 700 nm is required to excite SPPs with a minimal propagation distance of 50 μm. As demonstrated in figure 4.3, the excitation wavelengths employed are considerably smaller than the specified wavelength. Consequently, it is to be expected that no light can be seen at the tip. Nevertheless, a light can be seen. Once again, the propagation length offers a possible explanation. At the tip, SPPs that are excited below 700 nm then only have an amplitude of less than 1/e. These still decouple in the form of light, which can be detected. However, this does

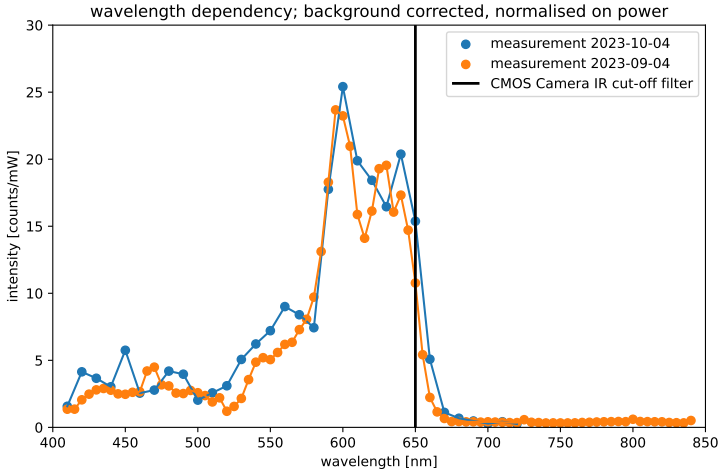

Figure 4.4: Background corrected and power-normalised intensity of the tip light depending on the excitation wavelength at the base side of the gold triangle. Additionally marked is the build-in IR short pass cut-off filter of the CMOS Camera

not provide an explanation for the observation in figure 4.3 that the light at the tip exhibits the same colour as the excited base side. This leads to the assumption that the tip light might be scattered light from the excitation laser.
Figure 4.4 shows a more detailed investigation of the dependence between the intensity of the tip light and the excitation light. The wavelength is varied from 420 to 840 nm with a bandwidth of 10 nm using the corresponding NKT monochromator. The ROI was evaluated as described in the methods section (3.2.2). Both measurements show a similar course. Small excitation wavelengths lead to low-intensity outcomes. With increasing wavelength, a rapid increase in the tip intensity can be observed. So this graph follows basically the theoretical expectations and the simulation of the propagation length of SPPs at the air/gold interface. As addressed before, the top-mounted CMOS camera has a built-in IR short pass filter that cuts off wavelengths above 650 nm. (see filter specifications at figure 6.1). Nonetheless, in accordance with the theory, SPPs with significant propagation lengths are expected from an excitation wavelength of 700 nm, which are not able to be observed by the filter.
This kind of measurement is repeated with the final setup described in section 3.2.3 to overcome the filter problem and get more sensitivity in the near-infrared region. The Andor iXon Ultra 897 camera is used as the detector unit (see sensitivity specifications in figure 6.3 in the Appendix). This camera has no built-in filter, a broader spectral range and a higher sensitivity than the CMOS camera. Furthermore, the

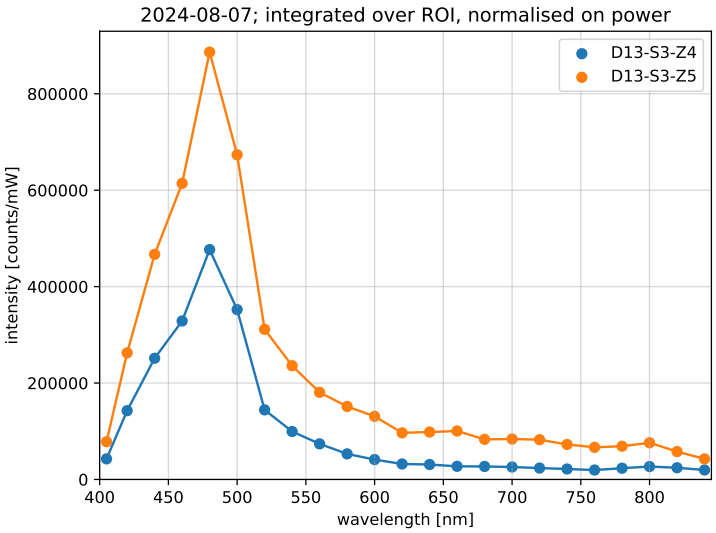

Figure 4.5: Background corrected and power-normalised intensity of the tip light as the function of the excitation wavelength. Triangles are 50 μm long and have a base width of 10 nm (**blue**) or 12 nm (**orange**). The Andor iXon camera is used as the detector

ROI can now be physically defined by the spatial selector. Figure 4.5 displays the obtained data with the final setup. As before, the measured data are divided by the power for each excitation wavelength for the purpose of normalisation. Please refer to the power-wavelength dependence in Appendix 6.5 for further details. Unfortunately, this measurement shows a different result compared to the first attempt with the CMOS camera. The graph shows a maximum at 480 nm for two different triangles. It can be assumed that the maxima are caused by the power normalisation. The power at the sample position is measured for each wavelength with a power meter. In comparison to other wavelengths within the range of 405 to 840 nm, the laser power at 480 nm is significantly smaller. The lower power additionally results in the excitation of fewer SPPs, which also have a significantly smaller propagation length compared to the length of the triangle. Therefore, a diminishingly low intensity is measured at the tip. In the event of two small values being divided by each other, the result is a very large value. So, a maximum occurs in the normalised data. A closer inspection at higher excitation wavelengths reveals that the normalised intensity slowly decreases. This doesn't fit with the expectations discussed in the theoretical section either. For a more detailed illustration of this intensity decrease, please refer to figure 6.6 in the Appendix.
Due to the small measured intensities for shorter excitation wavelengths, the nor-

malisation method does not provide meaningful data in this region through the creation of an artificial peak. For longer wavelengths, the data show no overlap with the theoretical expectation as well. So further investigation has to be done in this area. However, these measurements provide useful information. First, a detection method with a broad spectral resolution and high sensitivities is needed. Second, eliminating or at least considering disturbing influences, such as the IR filter. Lastly, the careful application of a correction or normalisation function to the measured data in order to obtain comparable data.

4.3 Spectral analysis

The previous approach did not experimentally show an exponential increase in intensity at the tip as a function of excitation wavelength. This section takes a different approach. As described in section 3.2.3 with the final version of the setup, it is possible to take a spectrum of an ROI. Therefore, the triangle base is illuminated with the entire available white light spectrum under grazing incidence. With the spatial selector, an ROI is selected at the position of the tip, and a spectrum of the light emission is taken with the spectrometer.

Correction and normalization spectrum

The previous section has shown the influence of the correction function. The measured data can be promising (fig. 4.4), but the needed data correction can generate misleading or meaningless results. So, the following sections discusses different approaches of correction and normalisation methods to obtain meaningful data.

Laser spectra

The expected spectrum at the tip S_{Tip} following equation 2.13, has shown that the excitation spectrum S_{Laser} must be taken into account. In order to obtain detailed information about the excitation spectrum, the white light spectrum of the laser was measured directly with the spectrometer. A known grey filter (Thorlabs NE50A) was used to avoid damaging the detector. Afterwards, the measured WL spectrum is corrected with the known filter spectrum to get the real WL excitation spectrum. The filter spectrum is taken from the manufacturer's specifications [39]. The following figure 4.6 shows the directly measured laser spectrum of the NKT extreme laser for a power output of 50% (blue line). This power output is equivalent

to the power used for the sample excitation. The red line reveals the corrected laser spectrum.

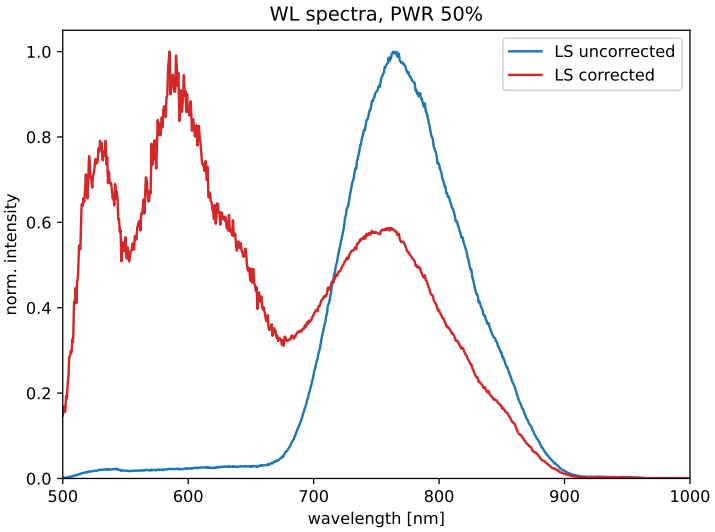

Figure 4.6: NKT extreme laser spectra at 50% power. **blue line:** measured spectrum with two Thorlabs absorption filters NE50A, **red line:** corrected laser spectrum

The measured spectrum shows a Gaussian-like shape with its maximum at around 780 nm. Unfortunately, the filter correction shifts the laser spectrum by around 150 nm to shorter wavelengths. Also, the overall shape has changed compared to the uncorrected spectrum. Multiple local minima and maxima have been created. A similar problem as in section 4.2 is assumed. The correction function has in the region from 500 and 650 nm very small transmission values. As mentioned before, when dividing two small numbers from each other, larger values result. It is, therefore, difficult to say whether figure 4.6 displays a mathematical artefact or the 'real' corrected laser spectrum.
In the following, the corrected WL-spectrum of the NKT-extreme laser (see fig. 4.6 red line) is used to normalise the measured tip spectrum.

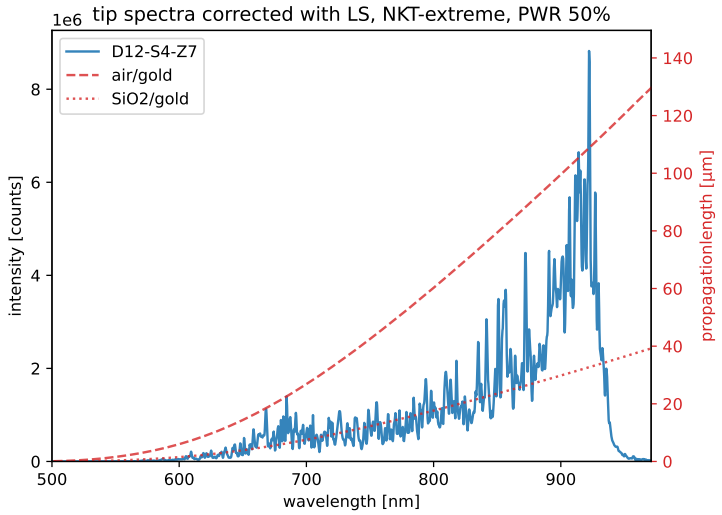

Figure 4.7: Correction of the measured tip spectrum of a triangle with length: 50 μm and base side width: 16 μm, **blue, left axis**: tip spectrum normalised with the directly measured NKT-extreme laser spectrum 4.6, **red, right axis:** Calculated propagation length of SPP's at air/gold (dashed) and SiO2/gold (dotted) interface

Figure 4.7 shows the intensity of the measured tip spectrum S_{Tip} as a function of the excitation wavelength, where the excitation spectrum has been taken into account. The calculated spectral propagation lengths $S_{\text{Propagation}}$ at both the air/gold and the SiO2/gold interfaces are depicted as well. The measured tip spectrum shows, under consideration of the laser spectrum, an increase in intensity in the red spectral region. This corresponds to the effect, which is already seen in figure 3.8. As mentioned before, the intensity at the tip and the calculated propagation length are connected by the exponential decay of SPP amplitude. However, in this particular instance, the proportion factor remains unknown. Assuming this connection, one can compare the shape of both data, shown in figure 4.7. In the region from 500 to 800 nm, the corrected data reproduce the course of the simulated SiO2/gold data. Up to 900 nm, the measured data deviate from the simulation data and approach the air/gold interface data with a steeper slope. Since the measured spectrum and the simulation follows the same shape and the light emitted at the tip is centred in the red spectral region, one can assume that its origin is a plasmonic nature.
The simulation for the penetration depths 2.2.2 has revealed that the penetration of the SPPs from both interfaces into the gold layer is larger than its thickness. One could assume that the excited SPPs of both interfaces interfere and influence

each other. Since the measured data lies between the simulation data, the light at the tip is probably based on the emission of the interfering plasmons. According to the good fit of measured data to the lower limit, the SPPs of the SiO2/gold interface are more dominant up to 800 nm. For the area between 800 to 900 nm, the weighting of the influence seems to be shifting more towards the SPPs excited at the air/gold interface. Since the properties of the SPPs of both interfaces are calculated separately from each other in the simulation, no prediction can be made about potential interference effects. So, figure 4.7 shows the first spectral resolution of the tip light under consideration of the excitation spectrum. The shape of the data follows basically the shape of the theoretical expectations. To verify the reproducibility of the method, it was applied to a second triangle with different dimensions (length: 30 μm, height 8 μm).

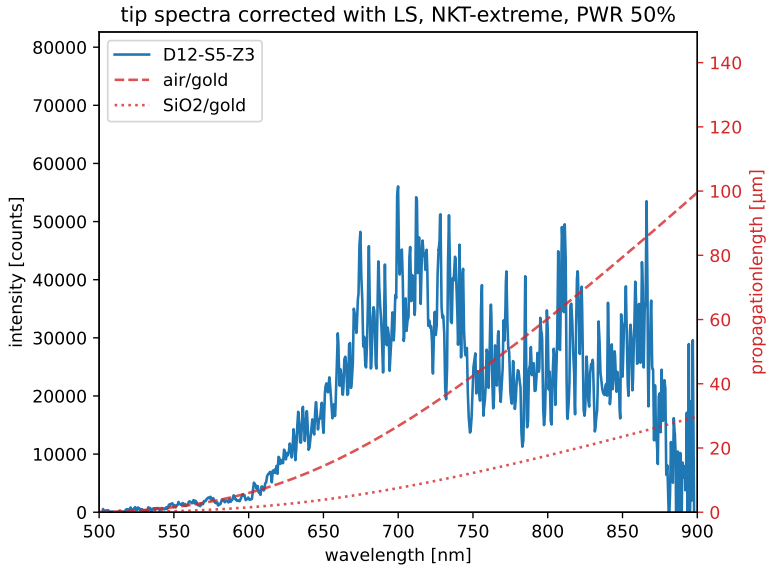

Figure 4.8: Correction of measured tip spectra of the triangle with other dimensions (length: 30 μm, width 8 μm), correction spectra is the measured white light laser from above 4.6

As demonstrated in figure 4.8, the corrected tip spectrum of a triangle with other dimensions (length: 30 μm, width 8 μm) exhibits a significant deviation from the previous measurement. The spectrum displays higher signal intensity in the red spectral range in comparison to shorter wavelengths. However, The spectrum shows a steep increase in intensity up to 700 nm, but the further shape is not in agreement with the shape of the theoretical predictions.

From one perspective, at this shorter triangle (length: 30 μm), it should be possible to excite SPPs at smaller wavelengths. From the other perspective, the excitation side and the observed ROI at the tip are closer together, which eventually allows more scattered light from the extended laser focus to reach through the spatial selector and hit the detector. However, given that the intensity measured in this case is 100x less than that recorded in the previous measurement (see Figure 4.8), this is improbable. A more appropriate explanation for the reduced recorded intensity is the width of the triangle base side. With 8 μm this triangle base has half the width of the previous triangle. As can be seen in figure 3.8, the laser spot fully illuminates the 16 μm wide triangle base. The laser spot is larger than the base width of the triangle used in figure 4.8. This results in a reduced area available for excitation, leading to a lower coupling efficiency, η_{Coupling}, which leads to fewer plasmons. This, in turn, gives rise to a smaller number of decoupling SPPs at the tip, which in turn results in less measurable intensity output.
The attempt to eliminate influence factors, such as the excitation spectrum S_{Laser}, is validated by the results of the previous measurements. Both measurements exhibit a significant increase in intensity towards the red spectral range. However, both measurements have a poor S/N ratio and show strong deviations from the predicted propagation length behaviour.
To possibly get a better accordance of data and theory, and a uniform shape of the measured data, one can try to eliminate losses caused by the setup through further normalisation.

Nanoparticle scattering spectra and laser-system-spectrum

Up to this point, in the previous approaches, only the detector sensitivities have been taken into account in the prediction of the spectrum to be expected. The losses and potential influence of the optical elements incorporated within the experimental setup have been neglected in the setup component L_{Setup} of equation 2.13. Furthermore, the measurement of the excitation spectrum directly at the laser output does not consider the losses caused by the optical elements in the grazing incidence path.
This section discusses another correction method, which considers the influence of the setup. The correction method is based on the scattering of the incoming light at known nanoparticles. So the scattered light takes the same way as the emitted light from the triangle tip and is exposed to the same losses.

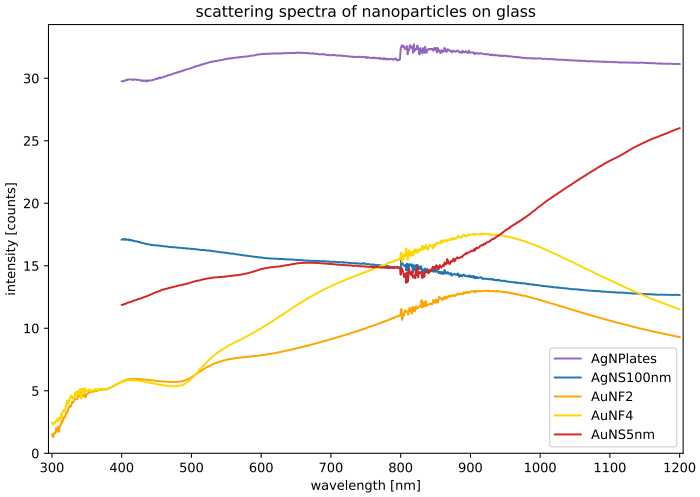

Figure 4.9: Scattering spectra of silver (100nm) and gold (5nm) spheres, silver nanoplates and gold nanoflowers measured with a UV-VIS-NIR spectrometer and an integrating sphere

To achieve this, samples with different nanoparticles on glass substrates are prepared. Afterwards, the scattering spectra of the samples are measured with a UV-VIS-NIR spectrometer and an integrating sphere. Figure 4.9 displays the different scattering spectra of the nanoparticles. After the measurement of the scattering spectra, the samples are placed in the setup 3.2.3 for SPP excitation. The different nanoparticles are illuminated under the same conditions as the triangles: white light excitation under grazing incidence with 50% power output of the laser. For each nanoparticle sample, a spectrum of the scattered light is taken with the Andor spectrometer. By correcting the spectrum measured with the Andor spectrometer with the corresponding scattering spectra of the nanoparticles (see figure 4.9), a laser-system-spectrum (LSS) is obtained. The LSS contains the excitation spectra and the losses from the setup. So the LSS contains detailed information for two components of the expected plasmon spectra. The excitation spectrum and the spectrum of the setup with the influence of the optical elements and the detector sensitivity ($S_{\mathrm{LSS}} = S_{\mathrm{Laser}}\, L_{\mathrm{Setup}}$)
Figure 4.10 shows the normalised laser-system-spectrum of the white light laser with 50% power output for three different nanoparticles. The normalised LSSs for the different nanoparticles look rather similar and have a Gaussian-like shape with their maxima between 650 and 700 nm. So this is the obtained laser-system-spectrum for GI-white-light excitation with 50% power of the NKT-extreme laser. In order to obtain comparable data, the same measured tip spectra are used as in

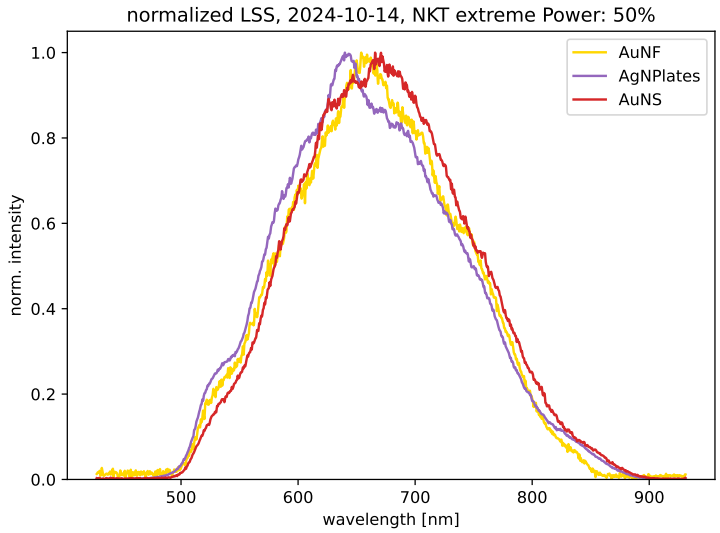

Figure 4.10: Normalised laser-system-spectra of the white light laser (power output: 50%) for silver nanoplates, 100 nm silver spheres and 5 nm gold spheres

section 4.3. In contrast to the previous section, the data are corrected with the laser-system-spectrum. Figure 4.11 displays the measured and LSS-corrected tip spectrum as a function of the excitation wavelength for the first triangle with the dimensions: length: 50 μm, base width 16 μm As before the calculations of the propagation lengths for both interfaces are displayed. In general, for excitation wavelengths up to 820 nm, the intensity increases, and its shape follows the shape of the theoretical predictions. For shorter wavelengths, the shape of the corrected data is in closer proximity to the shape of the simulation data from the SiO2/gold interface. From 650 nm to around 820 nm the data tends to approach the air/gold simulation data. Furthermore, a clear maximum at 820 nm can be seen in the red spectral range. Above this wavelength, the intensity starts to decrease.

The LSS correction of the measured data from the tip spectrum of the other triangle with different dimensional properties (length: 30 μm, height 8 μm) is also redone. The result is displayed in figure 4.12. The corrected tip spectrum for the second triangle shows a similar trend. However, in comparison to the first triangle, the shape is more fluctuating, particularly above 700 nm. An intensity increase is observed up to 850 nm, which follows the same shape as the theoretical predictions. Above this wavelength, the intensity decreases with strong fluctuations.

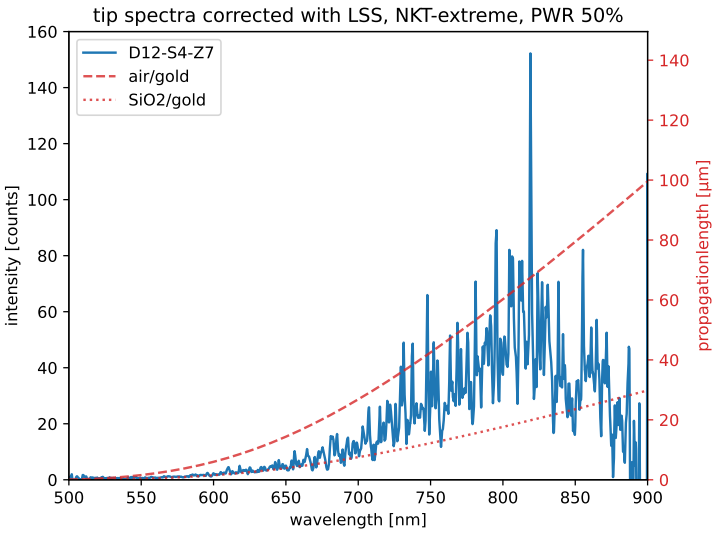

Figure 4.11: LSS-corrected tip spectrum (blue) of triangle with the dimensions: 50 μm, base width 16 μm. Simulation of propagation length of SPPs at air/gold and SiO2/gold interface (red lines)

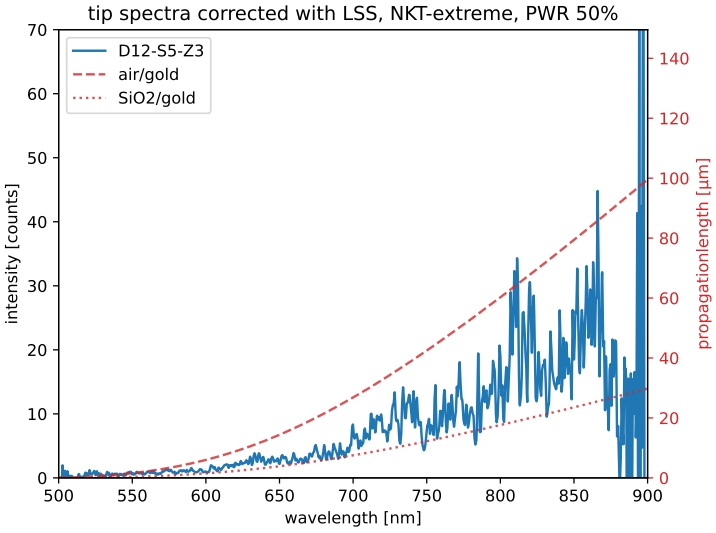

Figure 4.12: LSS-corrected tip spectrum of the second triangle (P12-C5-R3)

Both measurements demonstrate a significant intensity increase towards the red spectral region. Up to around 800 nm the shapes of the increase are in close proximity to the shape of the simulation data. However, the measured data do not precisely overlap with one of the theoretical curves but rather demonstrate a combination of both. As discussed in section 2.2.2, the thickness of the gold film is smaller than the penetration depth of the SPPs from both sides into the metal film. It is hypothesised that the SPPs of both sides will interact and interfere with each other. Therefore, it can be deduced that the measured data represents the combination of the SPPs from both interfaces. Furthermore, the discussion in section 2.4, predicts a decrease in the coupling efficiencies in the NIR spectral range. Consequently, a flatter slope of the propagation length is expected by considering the coupling efficiencies. These considerations match with the observed behaviour of the measured data with respect to the theoretical predictions.
For both measurements, the intensity decrease above 850 nm is unexpected. The decrease can not be explained by the influence and losses of the setup, as these are taken into account in this correction method. This leads to the suspicion that the coupling efficiencies exhibit another behavior than assumed, impacting the propagation behaviour as well, maybe even altering the shape of the function. However, much more elaborate simulations would be necessary to develop an adequate theory, so this will be the subject of future studies.

In contrast to the previous correction methods, the laser-system spectrum correction method takes all the discussed influence factors from equation 2.13 into account. The LSS-normalisation function eliminates both the excitation spectrum S_{Laser} and the losses of the setup L_{Setup} from the measured tip spectrum. Consequently, the propagation behaviour along the triangle and the coupling efficiencies at the edges remain, which are in detail discussed in the theory section 2.4. At two different triangles, an intensity increase in the red spectral region is experimentally observed. Furthermore, the shape of the increase is in agreement with the shape of the theoretical expectation. This strongly suggests that the observed light emission is of plasmonic nature.
The following section will discuss possible improvements for future investigations that can be made to acquire a better understanding of the excitation and propagation of SPPs on gold triangles.

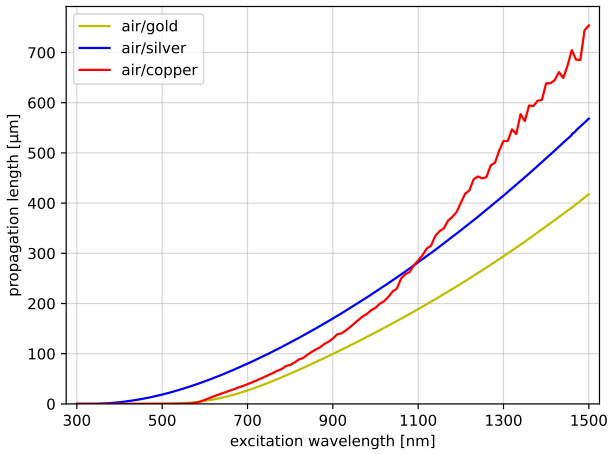

Figure 4.13: Simulated propagation length at different air/metal interface, in comparison to gold, silver shows [40] higher propagation length in the VIS and copper [41] in the NIR

4.4 Further Improvements

This section discusses further improvements and approaches that should be considered in future investigations to generate better and more promising results. First, the sample is no longer ideal due to the long usage time. Over time, a lot of dirt and other pollution sticks to the surface. Even strong cleaning methods like ozone plasma cleaning are not able to overcome the adhesion forces. Also a lot of triangles are broken or destroyed to mechanical damages during the different analysis processes. For future samples, the thickness of the gold layer should be significantly increased. This will increase the coupling efficiency, as shown by the calculations of Cruz et al. [34], as well by the work by Li & Zhang [33]. Also, the interference of the SPPs from both interfaces is prevented if the penetration depth into the metal is smaller than its layer thickness.
The usage of different metallic materials like silver [40] or copper [41] is currently being discussed. For example, in the visible region, the propagation lengths of SPPs at an air/silver interface are significant larger than at an air/gold interface [23] [36]. Up to around 900 nm, an air/copper interface provides similar propagation lengths as gold. However, the propagation length drastically increases for excitation wavelength in the NIR. The simulated propagation lengths for an air/silver and air/-copper interface are displayed in figure 4.13 alongside the simulation from section 2.2.3. So, triangles consisting of silver have larger propagation lengths in the VIS

region, which should provide better data in this developed VIS optimised setup. In contrast, copper is more suitable for the near-infrared spectra range. However, both materials have the problem of oxidization. The Santer group currently discuses the influence of silver oxide on the propagation behavior of SPPs at an air/silver interface.

In addition, the experimental setup can be improved in several ways. According to the theoretical calculations of the paper by La Cruz et al. [34], smaller angles of incidences with respect to the sample normal provide more coupling efficiency between light and SPPs. This can be achieved by using an objective with a larger working distance. An enhancement in the coupling efficiency results in a higher intensity of light extraction at the tip. The availability of greater intensity facilitates an increase in the range of analysis options, such as the utilisation of alternative spectrometers that exhibit reduced sensitivity but divergent spectral ranges. Furthermore, the pathway between sample and spectrometer is too long and runs over too many optical elements. Despite the infinite corrected objective, the optical beam diverges. Together with the optical losses at every element, this leads to a very weak signal and a small field of view at the detector.
But to overcome this issue, a complete rebuild of the optical setup is needed.
Lastly, the used detector is optimised for the visible region of the electromagnetic spectrum. But as seen in the result section, the detector reaches its limits above 950 nm. So, further investigations in the intersection from VIS to the near-infrared section are not possible. This spectral regime is in particular for longer gold or copper triangles of interest. In the future, detailed measurements in this area are only possible with a highly sensitive NIR spectrometer and the built-up NIR optimised pathway.

Another point of improvement is the calculation of the SPP properties. The simulations and calculations are performed for an infinitely extended and thick air and gold interface. Neither the geometry nor the layer thickness of the gold triangles are considered in the calculations. Furthermore, the calculations for both the interfaces are done separately form each other. So the simulations provide no information about the combined system air-gold-SiO2. Due to the high requirement of knowledge and skill, the calculation neglects the interference between the SPPs of both interfaces of the gold layer. All these points influence the properties of the SPP propagation along a gold nano-triangle. The goal is to achieve a wide-ranging simulation from a photon coupled to an SPP at a sharp edge structure over the propagation and focusing of the SPP along the triangle up to the usable energy at the triangle tip. In short, every part of the theoretical calculations can be improved for a better prediction of the SPP propagation.

5 Conclusion

In the context of this work a lot of theoretical and experimental investigations around propagating surface plasmon polaritons on gold triangles have been done. For this purpose, first I did some theoretical considerations about the properties and the behavior of pSPPs at an air/gold interface. This leads to the successful but simple modeling of the wavelength, penetration depth and especially the propagation length of the plasmons. In combination with estimations for the coupling between light and SPP, it was able to obtain a prediction for a expected spectrum at the tip.

For the experimental side I tried a lot of different approaches and investigation methods. Therefore a lot of improvements and expansions have been done on the setup. One of them, the grazing incidence white light excitations, looks very promising to excite SPPs at the air/gold interface of the triangle. For clarification polarisation- and wavelength-dependent measurements were done. The first measurement of the polarisation dependence fits to the theory, that a perpendicular electric field vector is needed for a successful excitation. For the wavelength dependent measurements some adjustments and deeper investigations has to been done. So I expanded the setup with a grazing incidence white light excitation, a spacial selector and a spectrometer with a high sensitive detector and imaging camera. With this final setup I was able to measure the emitted tip spectra. In combination with the used LSS-correction method, to take into account the excitation light and loss of the setup, I was able to obtain meaningful data. As shown above, this corrected data fits in principle to the theory.

These investigations have shown a first proof of concept to successful excite and focus pSSPs along the air/gold interface of nano triangles. Nevertheless to improve the efficiency and see clear correlations between the SPPs and the triangle properties, more and deeper investigations have to been done. Especially with regards to the goal of project A06 of the CRC1636, to drive chemical reaction by pSPPs far away from the excitation side. So this work is just the base stone to successfully drive a chemical reaction with propagating SPPs along a metal triangle.

In this final section I want to give a short outlook to future plans and other promising approaches all around pSPPs along metal nanostructures. First of all it is the goal to drive a chemical reaction with pSPPs far away from the excitation side. Two different dimerization processes are well known in the groups that work together in project A06 of CRC1636. On the one hand the dimerisation of 4NTP to DMAB by the UDKM group of Matias Bargheer [42]. On the other hand the dimerisation of azobenze based polymers by the SMM group of Svetlana Santer [23]. The goal is to drive the dimerisation process by a propagated and focused SPP which was excited several tenths of micrometer away at the baseside of the triangle. This dimersiation reaction can as well be assisted by the usage of upconversion particles provided by Michael Kumke. [43]
In addition to the excitation on the sharp edge of the triangle, also a grating excitation is possible. With further studies and a deeper understanding of the pSPP excitation and behavior, a grating excitation is more selective and adjustable to specific investigations, like limited excitation wavelengths or required energy regions. The technique to write gratings into metal films with AFMs is well known in the Santer group.
Lastly we are not limited to conceivable metal films. Thanks to modern 3D print techniques any thinkable structure of dielectrics can be made. This results in a large number of possibilities, like 3D printed dielectric triangle on a flat metal film.

6 Appendix

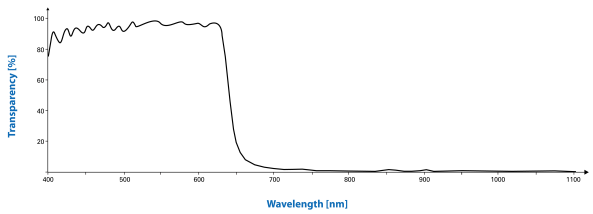

Figure 6.1: Fixed mounted IR Shortpass filter of the CMOS Camera. Cut-off wavelength around 650 nm [44].

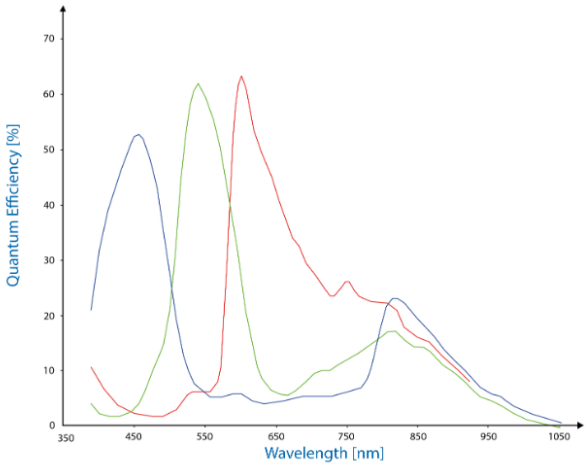

Figure 6.2: Sensitivity of the RGB CMOS detector chip [44]

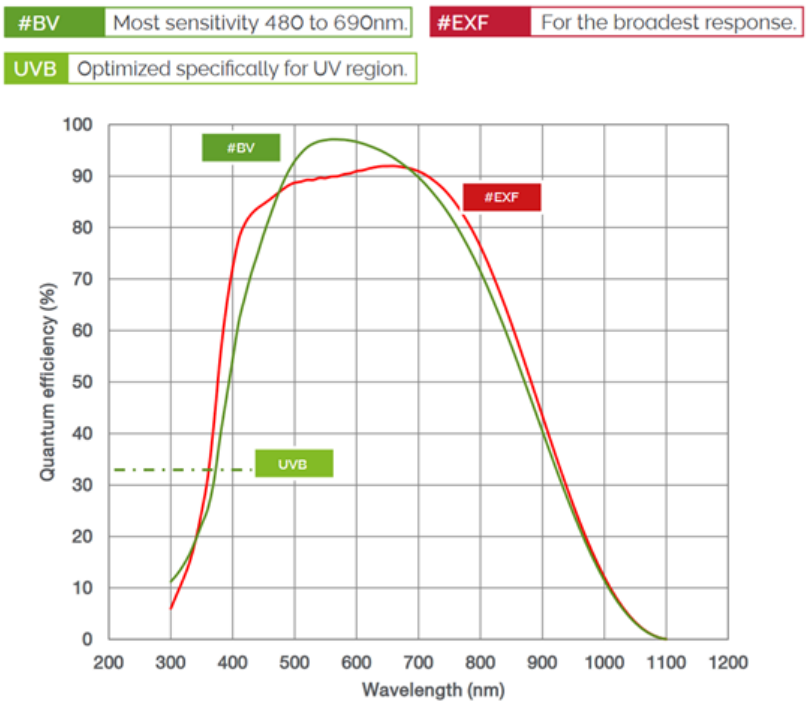

Figure 6.3: Quantum Efficiency of the Andor iXon detector depending on the wavelength [45]

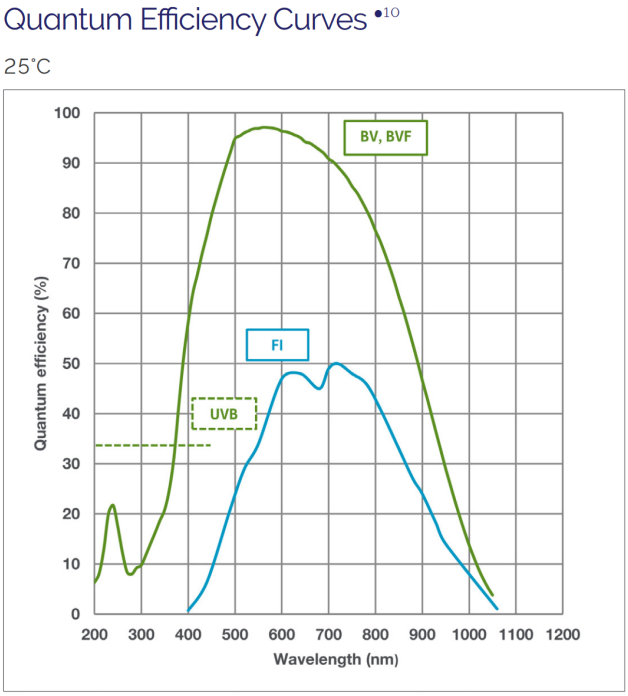

Figure 6.4: Quantum Efficiency of the Andor EMCCD DU970P-BVF detector depending on the wavelength [46]

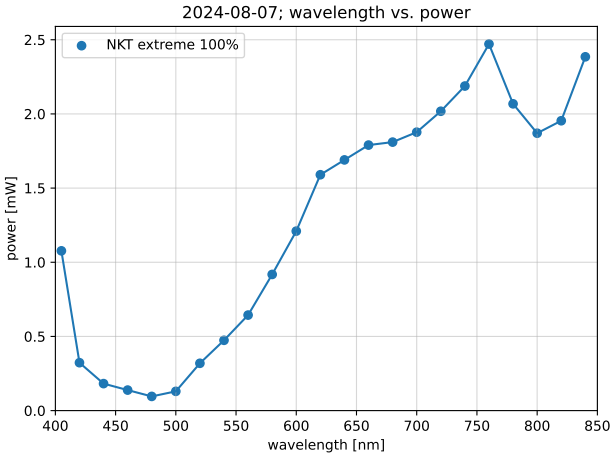

Figure 6.5: Measured power of the NKT extreme laser by 100%. Light is perpendicular linear polarised to the triangle base

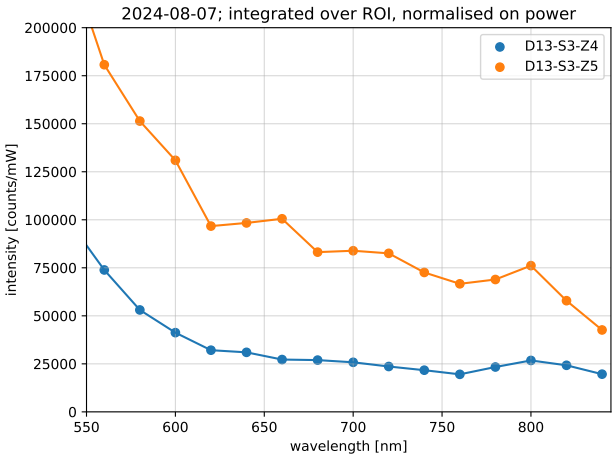

Figure 6.6: Wavelength-dependent measurement with the Andor iXon camera. selected region: 550 nm – 840 nm. The normalised date in this region shows a slowly decreasing intensity with higher excitation wavelength.

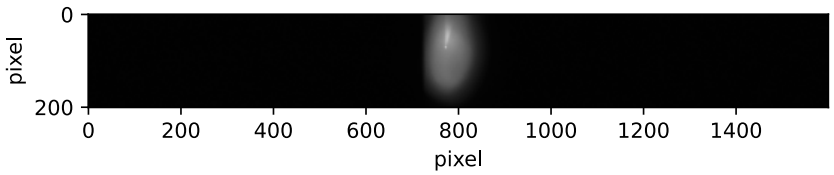

Figure 6.7: Full image of the 488nm laser at triangle tip (detector: Andor Newton EMCCD)

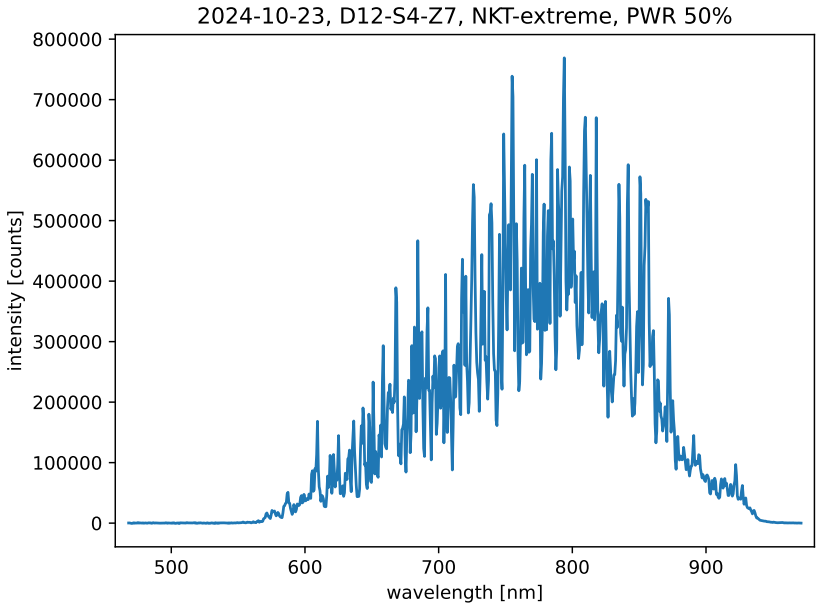

Figure 6.8: uncorrected tip spectra, P12-C4-R7, NKT-extreme 50% Power

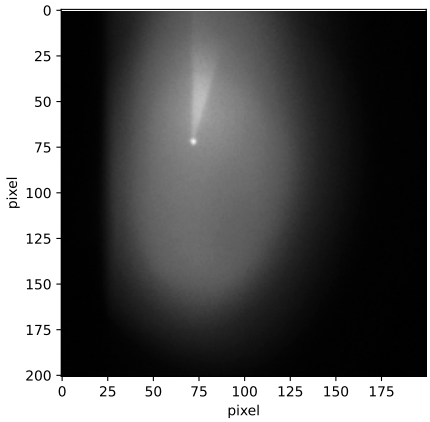

Figure 6.9: Region of Interest: triangle tip with 488 nm laserspot at Andor Newton detector. Additionally, you can see to the left side of the entry-slit of the spectrometer (x-axis: 25 px)

Bibliography

[1] S. A. Maier, **Plasmonics: Fundamentals and Applications**. Springer New York, NY, 2007 (see pages 1, 4–6, 13, 14).

[2] A. V. Zayats, I. I. Smolyaninov, and A. A. Maradudin, **Nano-optics of surface plasmon polaritons**, *Physics reports*, vol. 408:no. 3-4, 131–314 (see pages 1, 4).

[3] C. Ropers, **Femtosecond excitations in metallic nanostructures** (see pages 1, 4, 11).

[4] A. J. Babadjanyan, N. L. Margaryan, and K. V. Nerkararyan, **Superfocusing of surface polaritons in the conical structure**, *Journal of Applied Physics*, vol. 87:no. 8, 3785–3788, ISSN: 0021-8979. DOI: 10.1063/1.372414. eprint: https://pubs.aip.org/aip/jap/article-pdf/87/8/3785/19048273/3785_1_online.pdf. [Online]. Available: https://doi.org/10.1063/1.372414 (see page 1).

[5] J. Homola and M. Piliarik, **Surface plasmon resonance (SPR) sensors**. Springer, 2006 (see page 1).

[6] R. Chang, **Surface enhanced Raman scattering**. Springer Science & Business Media, 2013 (see page 1).

[7] T. Liebermann and W. Knoll, **Surface-plasmon field-enhanced fluorescence spectroscopy**, *Colloids and Surfaces A: Physicochemical and Engineering Aspects*, vol. 171:no. 1-3, 115–130 (see page 1).

[8] T. W. Ebbesen, C. Genet, and S. I. Bozhevolnyi, **Surface-plasmon circuitry**, *Physics Today*, vol. 61:no. 5, 44–50 (see page 1).

[9] W. L. Barnes, A. Dereux, and T. W. Ebbesen, **Surface plasmon subwavelength optics**, *nature*, vol. 424:no. 6950, 824–830 (see page 1).

[10] S. A. Maier, M. L. Brongersma, P. G. Kik, S. Meltzer, A. A. G. Requicha, and H. A. Atwater, **Plasmonics—a route to nanoscale optical devices**, *Advanced Materials*, vol. 13:no. 19, 1501–1505. DOI: https://doi.org/10.1002/1521-4095(200110)13:19<1501::AID-ADMA1501>3.0.CO;2-Z. eprint: https://onlinelibrary.wiley.com/doi/pdf/10.1002/1521-4095%28200110%2913%3A19%3C1501%3A%3AAID-ADMA1501%3E3.0.CO%3B2-Z. [Online]. Available: https://onlinelibrary.wiley.com/doi/abs/10.1002/1521-4095%28200110%2913%3A19%3C1501%3A%3AAID-ADMA1501%3E3.0.CO%3B2-Z (see page 1).

[11] T. W. Ebbesen, H. J. Lezec, H. Ghaemi, T. Thio, and P. A. Wolff, **Extraordinary optical transmission through sub-wavelength hole arrays**, *nature*, vol. 391:no. 6668, 667–669 (see page 1).

[12] M. Bargheer and et. al., **Collarborative research center crc 1636 - elementary processes of light-dricen reactions at nanoscale metals**. [Online]. Available: https://www.uni-potsdam.de/en/sfb1636 (see page 1).

[13] J. Krenn and J.-C. Weeber, **Surface plasmon polaritons in metal stripes and wires**, *Philosophical Transactions of the Royal Society of London. Series A: Mathematical, Physical and Engineering Sciences*, vol. 362:no. 1817, 739–756 (see page 1).

[14] Z. Zhang, Y. Fang, W. Wang, L. Chen, and M. Sun, **Propagating surface plasmon polaritons: Towards applications for remote-excitation surface catalytic reactions**, *Advanced Science*, vol. 3:no. 1, 1500215 (see page 1).

[15] F. Stete, **Gold at the nanoscale: Plasmon - exciton coupling and optical heating**, doctoralthesis, Universität Potsdam, 2020 (see pages 3, 5, 24).

[16] R. Gross and A. Marx, **Festkörperphysik**. Walter de Gruyter GmbH & Co KG, 2018 (see pages 5, 12).

[17] M. N. Polyanskiy, **Refractiveindex.info database of optical constants**, *Scientific Data*, vol. 11:no. 1, 94 (see page 5).

[18] R. L. Olmon, B. Slovick, T. W. Johnson, D. Shelton, S.-H. Oh, G. D. Boreman, and M. B. Raschke, **Optical dielectric function of gold**, *Phys. Rev. B*, vol. 86, 235147. DOI: 10.1103/PhysRevB.86.235147. [Online]. Available: https://link.aps.org/doi/10.1103/PhysRevB.86.235147 (see page 5).

[19] L. Gao, F. Lemarchand, and M. Lequime, **Exploitation of multiple incidences spectrometric measurements for thin film reverse engineering**, *Opt. Express*, vol. 20:no. 14, 15734–15751. DOI: 10.1364/OE.20.015734. [Online]. Available: https://opg.optica.org/oe/abstract.cfm?URI=oe-20-14-15734 (see page 5).

[20] H. Raether, **Surface plasmons on smooth surfaces**, *Surface plasmons on smooth and rough surfaces and on gratings*, 4–39 (see pages 6, 14).

[21] n.n, *W6 - Visualization of surface plasmons*, PPF Universität Potsdam, 2018 (see pages 7, 8, 25).

[22] J. Pitarke, V. Silkin, E. Chulkov, and P. Echenique, **Theory of surface plasmons and surface-plasmon polaritons**, *Reports on progress in physics*, vol. 70:no. 1, 1 (see page 7).

[23] T. Papke, N. S. Yadavalli, C. Henkel, and S. Santer, **Mapping a plasmonic hologram with photosensitive polymer films: Standing versus propagating waves**, *ACS Applied Materials & Interfaces*, vol. 6:no. 16, 14174–14180 (see pages 8, 25, 35, 36, 50, 54).

[24] P. Kahl, **Anregung, propagation, interferenz, photoemission: Oberflächenplasmonpolaritonen in zeitaufgelöster photoelektronenemissionsmikroskopie unter senkrechtem lichteinfall**, Ph.D. dissertation, Dissertation, Duisburg, Essen, Universität Duisburg-Essen, 2016, 2017 (see pages 9, 11–14, 35, 36).

[25] P. Berini, R. Charbonneau, N. Lahoud, and G. Mattiussi, **Characterization of long-range surface-plasmon-polariton waveguides**, *Journal of Applied Physics*, vol. 98:no. 4, 043109, ISSN: 0021-8979. DOI: 10.1063/1.2008385. eprint: https://pubs.aip.org/aip/jap/article-pdf/doi/10.1063/1.2008385/14959286/043109_1_online.pdf. [Online]. Available: https://doi.org/10.1063/1.2008385 (see page 11).

[26] S. A. Meyer, B. Auguié, E. C. Le Ru, and P. G. Etchegoin, **Combined spr and sers microscopy in the kretschmann configuration**, *The Journal of Physical Chemistry A*, vol. 116:no. 3, 1000–1007 (see page 12).

[27] A. P. Vinogradov, A. V. Dorofeenko, A. A. Pukhov, and A. A. Lisyansky, **Exciting surface plasmon polaritons in the kretschmann configuration by a light beam**, *Phys. Rev. B*, vol. 97, 235407. DOI: 10.1103/PhysRevB.97.235407. [Online]. Available: https://link.aps.org/doi/10.1103/PhysRevB.97.235407 (see page 12).

[28] B. Burrows and D. Colwell, **The fourier transform of the unit step function**, *International Journal of Mathematical Education in Science and Technology*, vol. 21:no. 4, 629–635. DOI: 10.1080/0020739900210418. eprint: https://doi.org/10.1080/0020739900210418. [Online]. Available: https://doi.org/10.1080/0020739900210418 (see page 13).

[29] N. Homonnay, **Oberflächenplasmonenresonanz an planen und strukturierten metalloberflächen**, Ph.D. dissertation, Dissertation, Martin-Luther-Universität Halle-Wittenberg, 2010, 2010 (see page 14).

[30] I. P. Radko, S. I. Bozhevolnyi, G. Brucoli, L. Martín-Moreno, F. J. García-Vidal, and A. Boltasseva, **Efficiency of local surface plasmon polariton excitation on ridges**, *Phys. Rev. B*, vol. 78, 115115. DOI: 10.1103/PhysRevB.78.115115. [Online]. Available: https://link.aps.org/doi/10.1103/PhysRevB.78.115115 (see pages 15, 18).

[31] T. Iqbal, **Coupling efficiency of surface plasmon polaritons: Far-and near-field analyses**, *Plasmonics*, vol. 12, 215–221 (see page 15).

[32] C. Ropers, C. C. Neacsu, T. Elsaesser, M. Albrecht, M. B. Raschke, and C. Lienau, **Grating-coupling of surface plasmons onto metallic tips: A nanoconfined light source**, *Nano Letters*, vol. 7:no. 9, PMID: 17685661, 2784–2788. DOI: 10.1021/nl071340m. eprint: https://doi.org/10.1021/nl071340m. [Online]. Available: https://doi.org/10.1021/nl071340m (see page 15).

[33] G. Li and J. Zhang, **Ultra-broadband and efficient surface plasmon polariton launching through metallic nanoslits of subwavelength period**, *Scientific Reports*, vol. 4:no. 1, 5914 (see pages 16, 19, 50).

[34] S. De La Cruz, E. R. Méndez, D. Macías, R. Salas-Montiel, and P.-M. Adam, **Compact surface structures for the efficient excitation of surface plasmon-polaritons**, *physica status solidi (b)*, vol. 249:no. 6, 1178–1187 (see pages 16, 17, 50, 51).

[35] R. A. Flynn, K. Bussmann, B. S. Simpkins, I. Vurgaftman, C. S. Kim, and J. P. Long, **Propagation length of surface plasmon polaritons determined by emission from introduced surface discontinuities**, *Journal of Applied Physics*, vol. 107:no. 1, 013109, ISSN: 0021-8979. DOI: 10.1063/1.3273480. eprint: https://pubs.aip.org/aip/jap/article-pdf/doi/10.1063/1.3273480/13649596/013109_1_online.pdf. [Online]. Available: https://doi.org/10.1063/1.3273480 (see page 19).

[36] I. Suárez, A. Ferrando, J. Marques-Hueso, A. Díez, R. Abargues, P. J. Rodríguez-Cantó, and J. P. Martínez-Pastor, *Nanophotonics*, vol. 6:no. 5, 1109–1120. DOI: doi:10.1515/nanoph-2016-0166. [Online]. Available: https://doi.org/10.1515/nanoph-2016-0166 (see pages 19, 50).

[37] *Fachgruppe nanostrukturierte materialien*, on page http://nano.physik.uni-halle.de/index.php (see page 21).

[38] R. A. Flynn, K. Bussmann, B. S. Simpkins, I. Vurgaftman, C. S. Kim, and J. P. Long, **Propagation length of surface plasmon polaritons determined by emission from introduced surface discontinuities**, *Journal of Applied Physics*, vol. 107:no. 1, 013109, ISSN: 0021-8979. DOI: 10.1063/1.3273480. eprint: https://pubs.aip.org/aip/jap/article-pdf/doi/10.1063/1.3273480/13649596/013109_1_online.pdf. [Online]. Available: https://doi.org/10.1063/1.3273480 (see page 29).

[39] *Thorlabs: Mounted absorptive neutral density filters*, Thorlabs. [Online]. Available: https://www.thorlabs.com/newgrouppage9.cfm?objectgroup_id=266&pn=NE50A#811 (see page 41).

[40] H. U. Yang, J. D'Archangel, M. L. Sundheimer, E. Tucker, G. D. Boreman, and M. B. Raschke, **Optical dielectric function of silver**, *Phys. Rev. B*, vol. 91, 235137. DOI: 10.1103/PhysRevB.91.235137. [Online]. Available: https://link.aps.org/doi/10.1103/PhysRevB.91.235137 (see page 50).

[41] K. M. McPeak, S. V. Jayanti, S. J. P. Kress, S. Meyer, S. Iotti, A. Rossinelli, and D. J. Norris, **Plasmonic films can easily be better: Rules and recipes**, *ACS Photonics*, vol. 2:no. 3, PMID: 25950012, 326–333. DOI: 10.1021/ph5004237. eprint: https://doi.org/10.1021/ph5004237. [Online]. Available: https://doi.org/10.1021/ph5004237 (see page 50).

[42] W. W. A. Koopman, R. M. Sarhan, F. Stete, C. Schmitt, and M. Bargheer, **Decoding the kinetic limitations of plasmon catalysis: The case of 4-nitrothiophenol dimerization**, *Nanoscale* (see page 54).

[43] S. Schimka, D. T. Klier, A. L. de Guereñu, P. Bastian, N. Lomadze, M. U. Kumke, and S. Santer, **Photo-isomerization of azobenzene containing surfactants induced by near-infrared light using upconversion nanoparticles as mediator**, *Journal of Physics: Condensed Matter*, vol. 31:no. 12, 125201 (see page 54).

[44] n.n., *DFK 72AUC02 - Technical Reference Manual*, The Imaging Source, 2019. [Online]. Available: https://www.theimagingsource.com/de-de/product/industrial/2u/dfk72auc02/ (see pages 55, 56).

[45] n.n., *iXon Ultra - The World's Highest Performance Back-illuminated EMCCDs*, Oxford Instruments. [Online]. Available: https://andor.oxinst.com/products/ixon-emccd-camera-series/ixon-ultra-897 (see page 56).

[46] n.n., *Andor Newton EMCCD - Market Leading Platform for Ultra- Sensitive & Ultrafast Spectroscopy*, Oxford Instruments. [Online]. Available: https://andor.oxinst.com/products/newton-ccd-and-emccd-cameras/newton-971 (see page 57).

Acknowlegdement

Firstly, I would like to thank Matias Bargheer. He gave me the incredible opportunity to work on a current hot topic in science and research, which enabled me to write this master's thesis. I would also like to thank my supervisor, Felix Stete, who always found time for me and provided so much support and advice during the preparation of my thesis. I also want to thank Bikash Das Mohapatra, who created the sample I used. Without him, this work wouldn't have been possible. I would also like to thank the whole UDKM working group for the friendly reception, delightful working atmosphere, and company.
Finally, I want to thank my family and my friends. Throughout this time, they have given me solid support and have always been there for me.

Selbstständigkeitserklärung

Hiermit erkläre ich, Gregor E. Stockmann, dass ich die vorgelegte Masterarbeit mit dem Titel *Investigation of surface plasmon polaritons on gold nanotriangles* selbst verfasst habe. Es wurde nur die angegebenen Quellen und Hilfsmittel verwendet. Diese Arbeit wurde in dieser oder ähnlicher Form noch keinem anderem Prüfungskomitee vorgelegt.

Ort, Datum

Gregor E. Stockmann